Transportation Geotechnics 42 (2023) 101105

Contents lists available at ScienceDirect

Transportation Geotechnics

journal homepage: www.elsevier.com/locate/trgeo

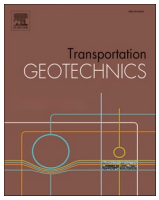

Experimental investigation of mixing railway ballast grains with different form using large-scale direct shear box apparatus

Ákos Orosz *, Zsolt Farkas, Kornél Tamás

Department of Machine and Product Design, Faculty of Mechanical Engineering, Budapest University of Technology and Economics, Műegyetem rkp. 3., H-1111 Budapest, Hungary

ARTICLE INFO

Keywords:
Railway ballast
Particle shape
Grain morphology
3D scanning
Large-scale shear box
Grain breakage

ABSTRACT

This paper investigates the effect of grain form on the mechanical behaviour of a railway ballast aggregate using large-scale shear box tests. The speciality of the research is that – contrarily to most of the experimental studies, where the shape content of the assemblies are not manipulated – here, the grains were carefully sorted and the ballast samples were assembled with the desired size and form content. A new sorting method was developed for laboratory-scale samples to separate compact and non-compact (flat, elongated or bladed) grains. This method utilises the combination of standard bar sieves and shape index calliper. The geometries of the grains in the resultant assemblies were thoroughly investigated using modern 3D imaging-based shape characterisation methods. With the adequate parameter thresholds, good correspondence was found between the standard industrial and the modern imaging-based methods, which allows the virtual reproduction of the introduced laboratory sorting technique. Three types of andesite railway ballast assemblies were tested experimentally: a fully compact, a fully non-compact and a mixed one. The mixed assembly had the highest internal friction angle which proves that it can be beneficial to mix grains with different types form. The amount of broken mass and the failure modes of the grains were also recorded, and it was found that the non-compact assembly had the highest rate of breakage. The results of the study also serve as a good basis for the calibration of numerical models.

Introduction

It is proven by several studies that the size and shape of the individual grains influence the mechanical behaviour of aggregates. Understanding the exact relationships will help to assemble more resistant structural aggregates with better lifetime. Grain shape is usually investigated at three different levels: overall *form*, *angularity* of the edges and *roughness* or *texture* of the surfaces [1]. This study is focused on the effect of form. (Note that in the literature *shape* is often used interchangeably with *form*, which is the roughest level of shape properties. To avoid confusions, the word *shape* will not be used in the present paper as a synonym for *form*, but as a general term for all geometry levels.) In an aggregate, besides the average shape of the particles, the distribution and proportion of different geometries are also of interest, as it has a significant influence on the strength of the assembly at the mesoscopic and macroscopic scales [2]. Objective characterisation methods are necessary to gain quantitative information about the geometry of the grains, while precise and efficient sorting methods are needed the assemble aggregates with the desired size and shape content.

Aggregates consists of irregular grains due to their nature and manufacturing processes, which makes their sorting and characterisation challenging, especially at industrial scales. Standard industrial methods often sacrifice some precision for economic reasons. Several industrial standards have been established to regulate the particle size distribution (PSD) of ballast. In industrial practice, the material is carefully sorted before its application using sieves with square apertures (e.g. ISO 3310-1 [3], Fig. 1 a), to maintain the desired PSD. The same method is used for characterisation of a sample. The only information that this method gives about the size of a single grain is its *fraction* i.e., its upper (the smallest hole size through which the grain can fit), and lower size bound (the largest hole size which retains it). The exact grain sizes between these two standard openings are not known and the PSD curve between is assumed to be linear. One can imagine that grains with various forms and sizes can have the same fraction. Considering grain shape characterisation, even rougher simplifications are made in the standards and in the industry and usually only form is investigated of the shape levels due to practical reasons. Grains are sorted into only two form groups in the European standards EN 933-3 [4] and EN 933-4 [5]

* Corresponding author.
E-mail address: orosz.akos@gt3.bme.hu (Á. Orosz).

https://doi.org/10.1016/j.trgeo.2023.101105
Received 5 May 2023; Received in revised form 1 September 2023; Accepted 3 September 2023
Available online 9 September 2023

based on whether they pass a special gauge (Fig 1 b and c) or not. The parameters that describe the form of the entire assembly are the mass ratios of the two groups (*flakiness index* for EN 933-3 and *shape index* for EN 933-4). Similarly to size characterisation with square sieves, precise form indices about single grains are not provided with these methods. The only information is that non-passing grains are towards a compact form (excluding elongated grains in the case of EN 933-3, but that will be discussed later). In contrast to the industrial practice, Zingg's classification system [6] distinguishes four form types based on two ratios of the three main grain dimensions. These categories are referenced as (there are a few variations in the literature) *compact/cubic/cube*, *flat/flaky/oblate*, *elongated/prolate* and *bladed/flat-elongated*. The almost a century old Zingg system is still often used to this day, see e.g. [7]. This notation will be followed from now on. The industrial approach enables the application of "go-no go" type of gauges, such as bar sieves [4], or a shape index gauge [5], which substantially reduces the time demand of the grading process, contrary to Zingg's system, where the three main dimensions of every grain have to be measured.

Several advanced methods have been developed to characterise grain shape, which take advantage of modern imaging techniques, like photogrammetry [8–10] including microscopic scales [11], 3D scanning [12–14] and X-ray computed tomography [15–17]. Thorough overviews of these methods are given in [18] and [19]. A further benefit is that many of the algorithms, which were originally created to process imaging data can also be utilised to characterise virtual grains in simulations (either created manually using direct definition, with the simplification of 3D scans or automatically using algorithms), allowing a direct comparison. Although 3D scanners and similar imaging technologies improve rapidly and there are promising developments, we are still far away from an industrial device that characterises every grain in real-time and sorts the aggregate based on that information. Hence, the results of algorithmic size and form characterisation methods are not identical to those that are used in the industry. The opinion of the authors is that focus should also be brought to industrial methods, as these are currently applied in real-life practice.

Experimental and numerical studies prove that non-compact grains tend to break more easily [7,20–23]. The majority of the numerical studies apply the discrete element method (DEM) [24]. This technique models materials with distinct elements with independent degrees of freedom. Interaction forces can rise and disappear between these elements [25]. Shi et al. [26] investigated numerically particle breakage during tamping, which is an aggressive intervention [27], and proposed that the ratio of flat and elongated grains should be limited to 20 % in the ballast aggregate. In the European standard EN 13450 [28], the maximum mass proportion of non-compact grains is 30 % if they are sorted with bar sieves and 35 % if they are sorted using a shape index gauge [29]. According to Deiros Quintanilla, "too flat" and "too elongated" particles should not be present in ballasted tracks at all to perform its functions [30].

However, there is an opposing effect: a plethora of studies prove that the deviation from compact form increases the shear strength of granular assemblies due to increased interlocking. Ying et al. [31] performed experimental shear box tests on geogrid-reinforced aggregates with different overall regularity and experienced that more irregular assemblies have higher shear strength. They did not investigate the effect of mixing grains with different form. Most of the shape-effect studies are numerical investigations because it is much easier to control and characterise the form of the grains in simulations than in experiments. Liu et al. [32] reported 2D DEM direct shear simulation test results, where a decrease of sphericity [33] (i.e. deviation from a sphere in 3D and from a circle in 2D, in the latter case it is also referred as *circularity*) increases the internal friction angle of the assembly. This behaviour has also been reproduced by Talafha and Oldal [34]. Zhao et al. [35] performed DEM simulations of triaxial tests and compared the shear behaviour of monodisperse spherical, polydisperse spherical and non-spherical assemblies. Their results show that the shear strength of non-spherical assemblies is substantially greater due to interlocking effects. It was also observed that the effect of size polydispersity was limited. Linero-Molina et al. [36] claim that grain form distribution has higher order factor in shear strength than the PSD. Contrarily, the industrial practice is different: the PSD has the primary role in aggregate characterisation and form is secondary. Usually, the aggregate is graded based on particle size, then samples are taken, and particle forms are only characterised as a quality measure.

Although DEM simulations offer a precise control over particle form and let insight to the micromechanical behaviour of granular aggregates, they still have to be calibrated and verified against experimental evidence. Full-scale tests are possible [37], however the three most widespread types of experiment to calibrate the parameters of DEM models in ascending precision order are *angle of repose*, *laboratory direct shear* and *triaxial shear tests*. Higher precision comes with a price: more accurate devices are more complex. This is even more significant when the grain sizes are large and unique large-scale instruments have to be custom-made. The angle of repose test is the least accurate, as a proven, direct link between the angle of repose and the internal friction angle of granular materials does not currently exist [38]. For example, some of these uncertainties entail that the repose angle is dependent on how the heap is formed [39] or how the angle is measured [40]. Suhr et al. reported that the same angle of repose can be reproduced by a wide range parameter values for the same simulation (i.e. the *parameter ambiguity* is high) [41]. The direct shear test has a drawback as well, as the position of the shear band is prescribed by the geometry of the apparatus, which might not be the weakest plane of the assembly. Furthermore, the theoretical stress and strain field of the grains (a horizontal shear plane is formed where the two halves of the shear cell meet) is far from reality [42,43]. Despite their disadvantages, laboratory direct shear tests are widely used, because they offer a good compromise between accuracy and complexity.

The two opposing effects (grain breakage and resistance against shear) suggest that there is an optimal form distribution. In other words,

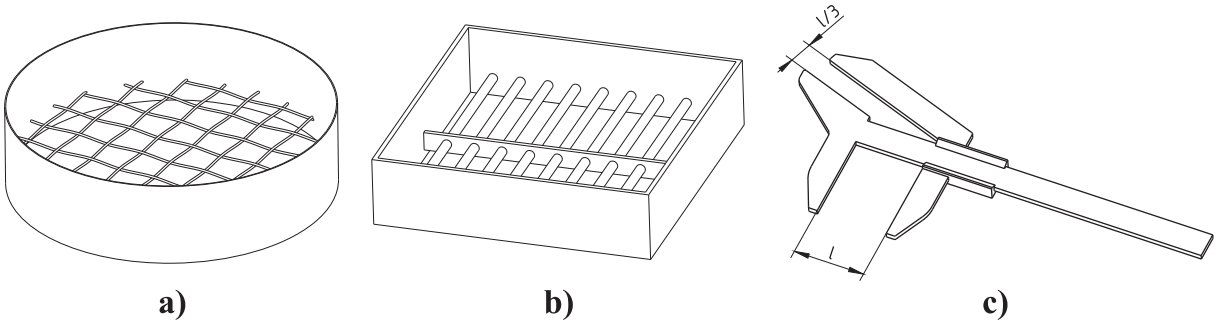

Fig. 1. Simplified 3D drawings of standard aggregate sorting devices: a) ISO 3310-1 square sieve (here 31.5 mm), B) EN 933-3 bar sieve (here 20 mm), c) EN 933-4 shape index calliper (*l* is the largest Feret diameter of the grain).

if we use industrial methods for classification, there is an optimal non-compact to compact grain ratio. This content is expected to be dependent on the material of the assembly and on the magnitude and mode of the load that it has to bear, because the interlocking effect may dominate at lower and grain breakage at higher stresses. This study focuses on the low load region, where the breakage rate is also low, and the interlocking effect dominates.

The majority of studies in the literature on the experimental testing of rock aggregates employ a large-scale direct shear test. Coetzee [44] performed direct shear tests on a crushed rock aggregate using a cylindrical (Jenike) shear cell with the purpose of using the measurements to calibrate a DEM model. The internal friction angle of the assembly calculated from measurements varied between 50.1° and 56.3° with an average of 52.8°. The aim of Suhr et al. [45] was also to calibrate a DEM model. Calcite from Croatia and Helvetic Silecious Limestone (i.e. "Kieselkalk") from Switzerland aggregates were sheared in a box. The secant friction angles of the aggregates were between: 53.5–64.6°. Linero-Molina et al. performed experiments to investigate the correlation between size and form in mine waste [36] using a large-scale shear box [43]. They recorded internal friction angles between 34° and 40°. They also highlighted the influence of gap size (i.e. the distance between the two halves of the cell) on the resistance against shear. Huang and Tutumluer [46] investigated the effect of fouling on a standard railway ballast material. The internal friction angle was 31° for the clean and 27° for the fouled assembly. Fischer and Horvát [47,48] investigated the effect of installing a geogrid [49] within a 1x1x1 m shear box. However, this device was not designed to bear high normal pressures, so the only load in their tests was gravity. Indraratna et al. studied both the effect of installing geogrids and fouling [50,51] and the internal friction angle in their tests was between 48 and 65°. Tanghetti et al. [52] designed a 1500 × 1500 × 1500 mm shear box. Li et al. [53] applied a circular shear box (504.6 mm diameter and 400 mm high plus a 15 mm shear seam) for soil-rock mixtures assemblies treated by different scaling methods and got friction angles between 17° and 35°. Further details of the reviewed direct shear experiments can be seen in Table 1.

Currently, the general opinion is that the amount of non-compact grains in a railway ballast assembly should be minimised, because they break more easily. However, their presence might be favourable under certain circumstances, as they increase the interlocking. Real railway ballast assemblies contain a mixture of compact and non-compact grains. In order to investigate the mechanical effect of non-compact grains, the ideal solution would be to test several assemblies with different compact/non-compact content. However, it would be extremely resource demanding to create and test such a high number of assemblies. Instead, it was decided to create one mixed assembly, one fully compact and one fully non-compact. The results of the latter two serve as a base of reference. The second reason of this choice is that further numerical studies are planned to extend the results of the experiments. Having data for assemblies consisting only one form category supports and accelerates the precise calibration of numerical models.

The general objective of this study is to contribute towards finding the optimal ratio of compact and non-compact grains by experiments and provide data for the calibration of DEM models, which can extend and refine the experimental results. This is done by fulfilling the following detailed aims. The first aim is to develop a precise and efficient form sorting method for aggregates that can be used to separate compact grains from non-compact ones. The second aim is to apply the method and characterise the resultant assemblies using different 3D imaging-based methods to gain detailed geometry data. The third aim is to give recommendations on how the results of the sorting method can be reproduced virtually, allowing its use for virtually generated granular assemblies. The final aim is to create three types of assemblies – a compact, a non-compact and a mixed one – with specified size and form content, shear them, then compare their macromechanical response and grain breakage characteristics.

Materials and methods

The new aggregate sorting method and its theoretical relation to bounding box-based characterisation systems

Many traditional standards rely on the three principal dimensions ($a > b > c$) of the particle, often referred as *length*, *width* and *height*, consecutively. They can be computed as the main dimensions of smallest cuboid in which the grain can fit (i.e., *oriented bounding box*, OBB). The retracted Hungarian standard, MSZ 18288-3:1978 [54], placed on each graph of Fig. 2 as a basis of comparison, is theoretically also based on the OBB. Although this standard is no longer in use, it still has value from the theoretical point of view. The three main dimensions of the OBB can be estimated by performing measurements of each grain using a simple calliper, which introduces a source of errors, because of high user-dependency in the measurements. The precision of the estimation of these dimensions is dependent on the experience of the measurement personnel. Moreover, the dimension a is often replaced by the largest measurable distance (i.e., Feret diameter) of the grain and dimension c is estimated as the smallest Feret diameter. The horizontal axis of the graph shows the ratio of the largest and intermediate principal dimension (a/b) of the OBB. Note that it starts at the value of one, as a is always bigger than b by its definition. The vertical axis represents the c/b ratio. Its value is between 0 and 1, because b is always larger than c but the axis

Table 1
Details of a few large-scale shear boxes from the literature.

Publication	Device parameters			Experiment parameters		
	Cell sizes (bottom + top half) [mm]	Max. normal stress [kPa]	Max. shear disp. [mm]	Shear velocity [mm/min]	Max. grain size [mm]	Normal stresses [kPa]
Indraratna et al. [50]	300 × 300 × 92.5 + 300 × 300 × 92.5	N/A	37	2.5	40	15, 21, 51, 75
Suhr et. al [45]	300 × 300 × 100 + 300 × 300 × 100	556*	40	1	40	111, 222, 333
Huang and Tutumluer [46]	407 × 305 × 152 + 305 × 305 × 53	537*	102	12	70	172, 241, 310
Coetzee [44]	Ø590 × 165 + Ø590 × 165	183*	70	60	40	10.5, 24.0, 38.3, 52.4
Linero-Molina et al. [36,43]	720 × 720 × 250 + 720 × 720 × 350	4000	150	N/A	100	500, 1000, 2000, 3000
Horvát et al. [48]	ten segments, each segment is 1000 × 1000 × 100	N/A	55	N/A	62.5	0
Tanghetti et al. [52] **	1500 × 1500 × 750 + 1500 × 1500 × 750	622	400	N/A	100	N/A
Li et al. [53]	Ø504.6 × 200 + Ø504.6 × 200	N/A	100	N/A	80	200, 400, 600, 800

* Calculated from the limit of the vertical force sensor which is 50 kN in each case. It is advised to apply only about the 80 % of the maximum force to ensure the safety of the cell.
** Design plan.

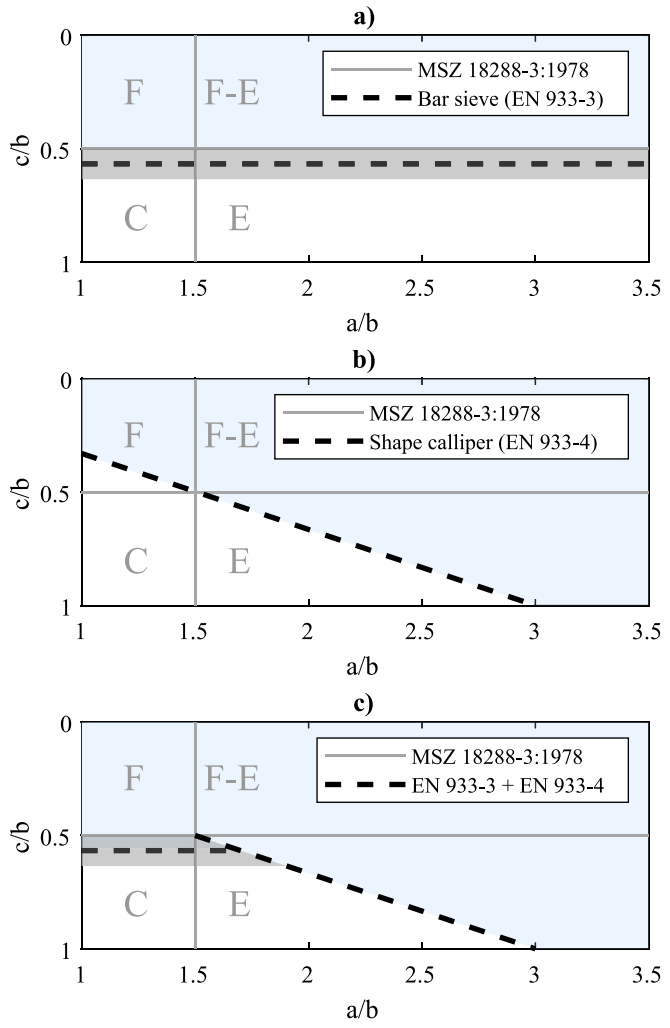

Fig. 2. Standard experimental grain form classification methods on an MSZ 18288-3:1978 type-graph: a) bar sieve, b) shape calliper method and c) the applied combined method, where $a > b > c$ are the principal dimensions of the oriented bonding box (OBB) of the grain and the region names are: C: compact, E: elongated, F: flat, F-E: flat-elongated. The grey area is the size-dependent region of the bar sieve, and the light blue region is the domain where the grains are classified as non-compact. (For interpretation of the references to colour in this figure legend, the reader is referred to the web version of this article.)

is inverted in the original standard for practical reasons. There are four types of grain form in this standard: *compact* (C), *flat* (F), *elongated* (E) and *flat-elongated* (F-E). There are two boundary lines which distinguish the four categories, at $a/b = 1.5$ and at $c/b = 0.5$ (Fig. 2).

Measuring the three principal dimensions with simple callipers takes a significant amount of time, therefore special gauges were developed, e.g. bar sieves (Fig. 1 b) and shape-index callipers (Fig. 1 c), following the European Standard EN 933-3 [4] and 934-4 [5]. The aperture size of the corresponding bar sieve for each size fraction is half the maximum size (e.g. a 25 mm bar sieve for the 40/50 fraction and a 20 mm bar sieve for the 31.5/40 fraction). Following this standard, the sieve sizes of the grains were approximated by their b value, and the aperture of the bar sieve is assumed to be equal to c. The bar sieve has an uncertainty in the c/b ratio threshold because a range of different sized grains are sorted with the same device (31.5–40 mm with the 20 mm sieve and 40–50 mm with the 25 mm sieve). The extrema are as follows: when a 50 mm grain just passes the 25 mm bar sieve, its c/b ratio is 0.5, and $c/b = 0.635$ if a 31.5 mm grain just passes a 20 mm sieve. Therefore, depending on the grain size, the boundary line using the bar sieve is somewhere between $c/b = 0.635$ and 0.5. The mean of these values is 0.567. This average c/b ratio line of the bar sieve is indicated by the dashed line in Fig. 2 a), and the other possible values (*size-dependent region* from now on) are marked by grey shading. Note that the application of bar sieves produces two groups: a compact/elongated and a flat/flat-elongated assembly.

The difference between a simple calliper and the shape index calliper is that the latter has two openings: a smaller and a bigger one. The size of the smaller opening is always equal to one third of the bigger one [5]. During sorting, the shape calliper is firstly adjusted so that its bigger opening matches the largest dimension ($\approx a$) of the grain. Then, it is tested whether the grain can pass the smaller opening (which is determined by its smallest dimension, which approximately equals c. Therefore, the shape calliper divides the assembly into two groups at $a/c = 3$. When this criterion is plotted in Fig. 2. b), it becomes a line with a slope of 1/3 which crosses the horizontal axis at the value of 3 (see the dashed line). Note that with shape calliper method, a large portion of the elongated grains will fall into the "passing" assembly, while a minor portion of the flat grains will not pass the gauge.

A clear advantage of the bar sieve is its efficiency because it can be applied at industrial scales, similarly to square sieves. However, its significant drawback that it does not separate the elongated grains from compact ones. Contrarily, the shape index calliper's passing assembly contains the large portion of the elongated grains, but it is not as efficient as the bar sieve as it requires human labour. An ideal sorting method would follow the MSZ 18288-3:1978 standard and would divide the grains into four groups: compact, flat, elongated and flat-elongated. However, this would be only possible with the time-consuming and subjective simple calliper method, hence that option was abandoned. Based on further aims it was also decided that two form categories, and *compact* and a *non-compact*, are sufficient for shape-effect experiments in the future. This decision was also supported by the experience of the authors is that non-compact grains (especially flat-elongated ones) are relatively rare in natural aggregates, hence it would require enormous effort to collect enough grains for a test. Ideally, the non-compact assembly would contain all flat, elongated and flat-elongated particles. The closest we could get this result was by combining the bar sieve and the shape index calliper method (Fig. 2. c), which was chosen as the new sorting method. This combined method is a good compromise between accuracy and efficiency, because the aggregate is firstly sorted by the bar sieves and only the remaining, non-passing grains had to be inspected by the shape index calliper. Experienced measurement personnel can further improve the efficiency by visually selecting the obviously compact grains after the application of the bar sieve.

About 40 years before the MSZ 18288-3:1978 standard was introduced, Zingg [6] proposed a slightly different diagram (Fig. 3), where the horizontal axis shows the c/b ratio and the vertical axis shows the b/a ratio. Both axes of the Zingg diagram start at zero and ends at one. Zingg also differentiated four types of grains, namely *compact*, *flat*, *elongated* and *bladed* (which is corresponding to the *flat-elongated* notation of the MSZ 18288-3 standard). The two threshold lines lie at $c/b = 2/3$ and $b/a = 2/3$. All the three introduced criterions (MSZ 18288-3:1978, EN 933-3 and EN 933-4) can be transformed and plotted on the Zingg diagram (Fig. 3). Note that the boundary between the F-C and B-E grains is the same in the case of the Zingg and the MSZ 18288-3:1978 systems (Fig. 3 a), but the same is not true about the boundary between the E-C and F-B region. Another similarity between the Zingg, MSZ 1828-83:1978 and EN 933-3 systems is that they divide the F-B and C-E grains with vertical lines (Fig. 3 b), i.e. based on constant values of c/b and b/a, but the specific value of the thresholds are slightly different across standards. The EN 933-4 line becomes a hyperbola with an equation of $b/a = 1/(3 \bullet c/b)$ on the Zingg plot (Fig. 3 c). The combined method can be seen on Fig. 3 d. The blue shaded areas represent the domain of the non-compact grains, similarly to Fig. 2.

Besides the traditional indices of Zingg, more recent form characterisation systems were applied as well during the evaluation of the 3D scans. Angelidakis et al. [55] pointed out that the domain of the bladed

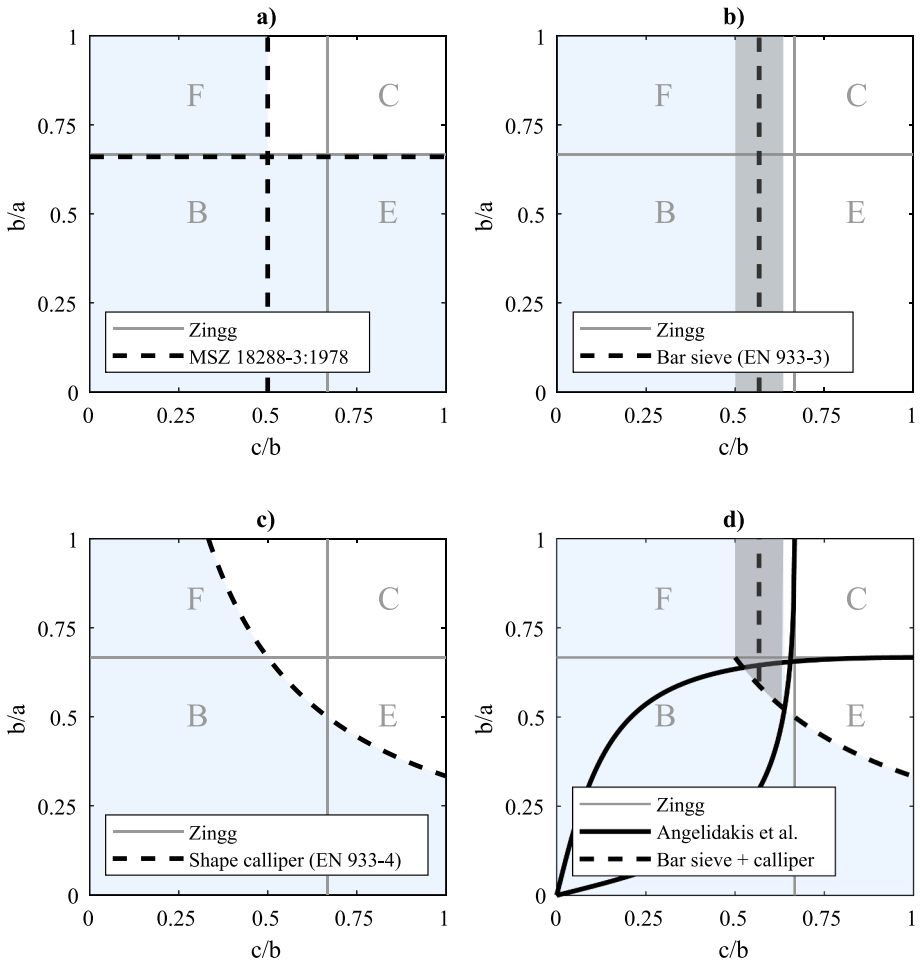

Fig. 3. A few grain form classification methods on a Zingg [6] type graph: a) MSZ 18288-3:1978, b) bar sieve (EN 933-3), c) shape calliper method (EN 933-4) and d) the applied combined method along with the system of Angelidakis et al. [55], where a > b > c are the principal dimensions of the oriented bonding box (OBB) of the grain and the region names are: C: compact, E: elongated, F: flat, B: bladed. The grey area is the size-dependent region of the bar sieve, and the light blue region is the domain where the grains are classified as non-compact. (For interpretation of the references to colour in this figure legend, the reader is referred to the web version of this article.)

grains of the Zingg classification system might be too broad, building on the observations of Sneed and Folk [56]. After reviewing existing sets of indices to characterise particle form, they proposed new formulae to compute elongation and flatness indices:

$$flatness = \frac{b^2}{a \bullet c + b^2} - \frac{c}{a + c} \quad (1)$$

$$elongation = \frac{a \bullet c}{a \bullet c + b^2} - \frac{c}{a + c} \quad (2)$$

The boundary lines between different form types in this system can also be mapped on a Zingg-type plot. If both elongation and flatness equal 0.2, the boundaries of the compact (upper right) region are similar to the Zingg classification, but the bladed region is much narrower (Fig. 3 d).

Test method of the new sorting technique, digital imaging

A standard EN 13450 [28] 31.5/50, grade A, grey andesite railway ballast aggregate from a quarry in Tállya, Hungary was chosen as the studied material. The designation "31.5/50" refers to the grain sizes in mm, but does not mean that the smallest grains have 31.5 mm square sieve size, and the largest ones have 50 mm. Because, according to the standard, the particle sizes in such an aggregate can range from fines to 63 mm. To have better control over the grain size, as the first step, the aggregate was sorted employing sieves with square openings according to EN 565:1990 [57] and only two gradations were kept: 31.5/40 and 40/50. Then, the grains were sorted based on their form. As a second step of the sorting process, the bar sieves were applied: the 40/50 grains were classified with a bar sieve having 25 mm apertures, and the 31.5/40 aggregates was classified with a 16 mm bar sieve. In a third step, each remaining compact grain was classified with a shape index gauge. Aggregates from the same size category which were classified as non-compact using different apparatuses were merged into one category. The process resulted in four aggregate categories: 31.5/40 compact (noted as "C31.5/40" hereinafter), 31.5/40 non-compact ("NC31.5/40"), 40/50 compact ("C40/50") and 40/50 non-compact ("NC40/50"). Samples were taken from the four different aggregate groups after the sorting: 25 particles were randomly chosen from each group, resulting into 100 analysed grains (25 pc. C31.5/40, 25 pc. C40/50, 25 pc. NC31.5/40 and 25 C40/50) altogether. Each grain received an identification number, therefore their group of origin was known. These 100 grains, shown in Fig. 4, were analysed in this study. The heights of the grains are hard to capture on a single photograph, but one can have a perception about the height differences between the grains by observing the length of their shadows (the assemblies were photograph with the same light source and direction).

The first step of the sorting process was sorting the grains based on their sieve size. Therefore, although this study is focused on grain form, it is also important to replicate the sieving process digitally. Digital imaging enables to get the size of every grain, but it is difficult to replicate the results of industrial sieving with algorithms. It possible to explicitly simulate the full sieving process using the DEM, as in [58], but it is ineffective for the analysis of large assemblies, composed of several thousand particles. Several simpler algorithms have been developed, based on geometrical measurements of the particles, e.g. in [17,59–61]. A popular approach was tested in this study, which is to use the principal dimensions of the OBB (based on smallest volume) of each grain.

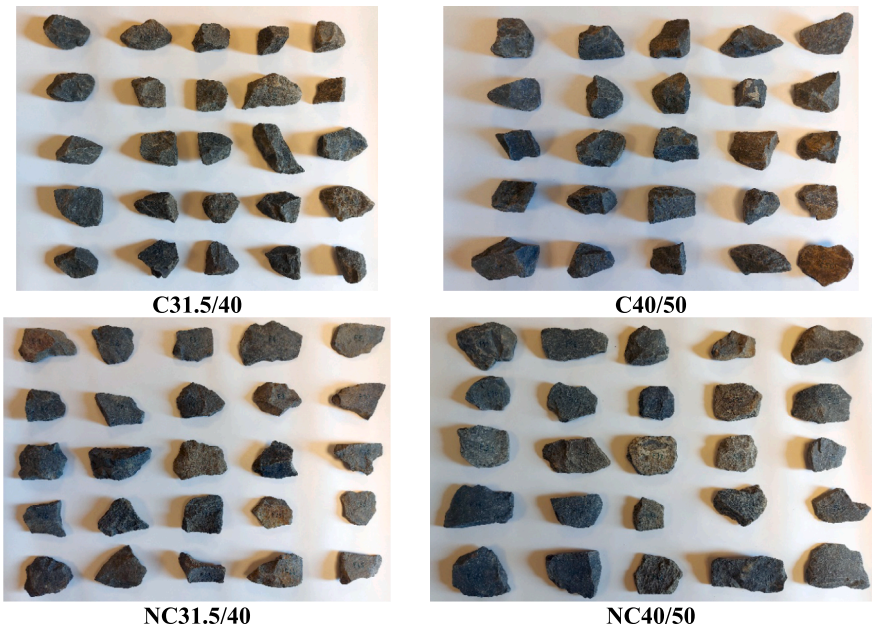

Fig. 4. The tested railway ballast specimen. C31.5/40: compact grains from 31.5 to 40 mm sieve size, C40/50: compact grains from 40 to 50 mm sieve, NC31.5/40: non-compact grains from 31.5 to 40 mm sieve size, NC40/50: non-compact grains from 40 to 50 mm sieve size.

Fonseca et al. [60] reported that "the match between PSD curve from sieving and the distribution of intermediate principal dimension is very good" for natural sands. Therefore, the sieve size (D) is simply: $D = b$ in their method. Ohm and Hryciw [61] proposed that the diagonal of the square sieve should be equal the diagonal of the smallest face of the OBB, therefore:

$$D = \sqrt{\frac{b^2 + c^2}{2}} \tag{3}$$

Further shape characterisation systems were applied as well to test the sorting method elaborately. Zingg's b/a ratio is inversely proportional to the elongation, while the c/b ratio is inversely proportional to the flatness of a particle. However, Zingg did not explicitly call these ratios "flatness" and "elongation", contrary to a few recent studies [55]. The inverse proportionality is counter-intuitive, therefore Kong and Fonseca [62] modified the original definition by subtracting the ratios from unity, and then called these flatness and elongation:

$$flatness = 1 - \frac{c}{b} \tag{4}$$

$$elongation = 1 - \frac{b}{a} \tag{5}$$

There are also systems which do not make use of the OBB. Potticary et al. [63] assigned a corresponding scalene ellipsoid instead of a cuboid (OBB) to ballast grains and computed two form indices. Using the principal axes of this ellipsoid ($L > I > S$ which are analogous to the principal dimensions of the OBB: $a > b > c$) as characteristic dimensions the form indices are calculated as:

$$flatness = \frac{2(I - S)}{L + I + S} \tag{6}$$

$$elongation = \frac{L - I}{L + I + S} \tag{7}$$

To eliminate the uncertainties of using an OBB to estimate the main particle dimensions of irregular particles, Bagi and Orosz proposed a form characterisation method [64,65] that computes three form indices (*compactness*, *flakiness/flatness* and *elongation*) directly from the raw surface mesh of a particle. This approach eliminates the approximation of characterising particle form based on three main particle dimensions, as for irregular particles this can lead to oversimplification of the problem. Firstly, the *surface orientation tensor* (SOT, f_{ij}) is computed, which is a modified fabric tensor [66], while it can also be seen as one of the Minkowski [67] tensors of the particle surface:

$$f_{ij} = \frac{1}{\sum_{(k)} A^{(k)}} \sum_{(k)} \left(A^{(k)} n_i^{(k)} n_j^{(k)} \right) \tag{8}$$

where $A^{(k)}$ are the face areas of the surface segments (triangles in most cases), $n^{(k)}$ are their orthonormal vectors, index (k) runs along all faces of the grain and i an j tensor indices ranging from 1 to 3. Note that similar tensors are often used the characterise the anisotropy of the fabric or void fabric network in granular assemblies [35,68]. However, the SOT defined by Bagi and Orosz applies to single grains. Three form indices can be calculated from the eigenvalues ($f_1 > f_2 > f_3$) of the SOT as follows:

$$Compactness = \frac{f_3}{f_1} \tag{9}$$

$$Flakiness = \frac{f_1 - f_2}{f_1} \tag{10}$$

$$Elongation = \frac{f_2 - f_3}{f_1} \tag{11}$$

The values of the three form indices always add up to one, therefore they can be visualised on a triangular (i.e. ternary) plot (see Fig. 9).

The grains were scanned with a DAVID SLS-3 structured light scanner (S/N 0004642). The maximum resolution of that device is 0.05 mm in ideal conditions according to the manufacturer, but it also depends on the size of the scanned object. Small, random bumps were observed on the surface of the scans with an average height of about 0.2 mm and a maximum height of 0.5 mm. The real precision was determined by the size of these bumps, hence the resolution of the scans was about 0.5 mm. This level of accuracy is sufficient to study particle form, it is adequate to characterise angularity, but it is too rough to characterise surface roughness.

Each single grain was represented with 1–2 million surface points. These were triangulated using the native software (DAVID 5) of the

scanner, resulting in 2–5 million triangles making the surface of each particle. Such high number of triangles is computationally challenging to process effectively, therefore the resolution was reduced to 100,000 triangles using the quadric edge collapse function of PyMeshLab [69], a Python interface of Meshlab, an open-source software for mesh manipulations. The tessellation of each particle surface was corrected of all faults (such as duplicate faces and vertices, non-manifold geometry, self-intersecting faces, holes) and these elements were checked and removed within PyMeshLab. The simplified 3D images were processed using SHAPE [70], an open source, MATLAB-based software for particle shape characterisation. SHAPE analyses the morphology of three-dimensional particles in an automated manner, with minimal human-intervention, based on imaging data of various types, while it calculates several groups of shape indices proposed in the literature. By default, this program automatically performs a repair on the analysed surface, performing tasks such as removing isolated elements, i.e. small triangles that are not connected to the main geometry, but it did not find any further faults in the particle shapes analysed here, as these repairs had already been carried out by PyMeshLab. Therefore, SHAPE was only used to calculate several geometry parameters.

An error number was defined to quantify the deviance of imaging-based characterisation methods from the applied physical sorting method. Hereinafter, the grains with 31.5/40 sieve size are referred to as *small*, and the 40/50 grains as *large*. Note that half of the analysed grains (50 pieces) were small and half of them was large according to the physical sorting method. Therefore, if their geometry indices are computed, the size of the small grains should be below the median size of all 100 grains (both small and large), and the size of the large grains would have to be above it, irrespective of the applied size characterisation method provided that the method is perfectly corresponding the physical sieving. The same applies to the form of the grains, namely half of them was compact, half of them was non-compact and their non-compactness value should be above the median if they are non-compact. The fulfilment of this condition was evaluated to test different sizing methods, so that if it is not satisfied, the grain is considered as falsely classified. It was also accounted that the indices of the falsely classified grains are how far from the median value. Based on these considerations, the defined error number (ε) is as follows:

$$\varepsilon = \sum_{i=1}^{N} |m - D_i| \tag{12}$$

where N is the number of falsely classified grains, m is the median value of the studied index, and its actual value is D.

Large-scale shear box apparatus

A unique laboratory large-scale shear box apparatus (Figs. 5 and 6) was built in the Laboratory of Building Materials and Building Physics at Széchenyi István University of Győr, Hungary, as part of this study. The shear cell was uniquely designed and manufactured for this study by welding 30 mm thick steel sheets. According to ASTM D3080 [71], the minimum width of the shear cell is 10 times and its minimum height is 6 times the size of the largest grain in the tested assembly. Because the sieve size of the largest grain is 50 mm, the inner dimensions of the cell were chosen to be 500 × 500 × 300 mm. The cell was placed on a set of rollers and the modular frame was adjusted to accommodate it. The normal and shear forces were exerted with a custom, manual and analog hydraulic system with two independent circuits. Analog hydraulics provided a robust and cheap alternative of servo-controlled systems at the cost of that normal forces had a slight variation. The magnitude of the normal force was adjusted with a pressure control valve and the shear velocity of the lower half of the cell was regulated with a manually adjusted aperture. During the design phase of the shear box apparatus, the aim was to keep shear velocity under 1 mm/s in all circumstances. This aim was fulfilled, with shear velocity varying between 0.1 and 1 mm/s (excluding one case, when it jumped to 1.4 mm/s for a short amount of time) with an average value of 0.33 mm/s. The measured strength of the aggregate is dependent on the freedom of the upper half and the size of the gap between the two halves [43]. During the first few

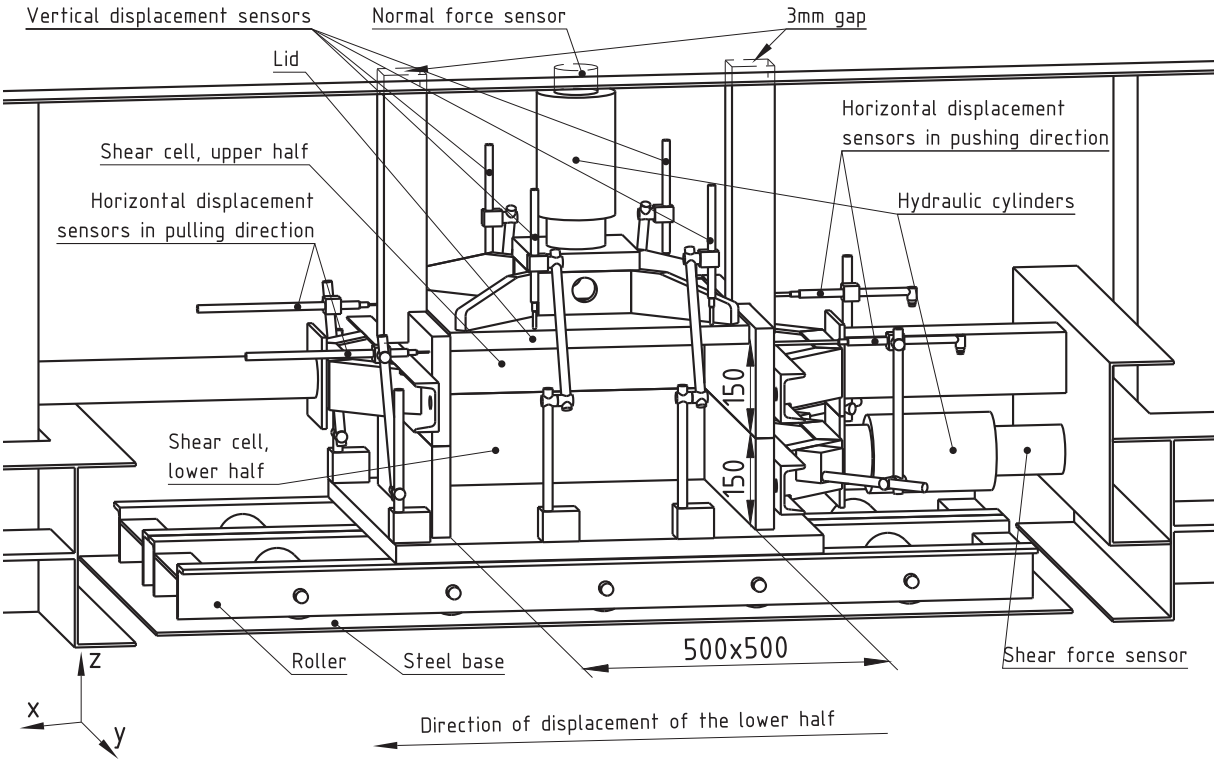

Fig. 5. Simplified 3D schematic of the large-scale shear box apparatus and the applied coordinate system. The right walls of the shear cell are hidden to show the inner dimensions [mm] of the box.

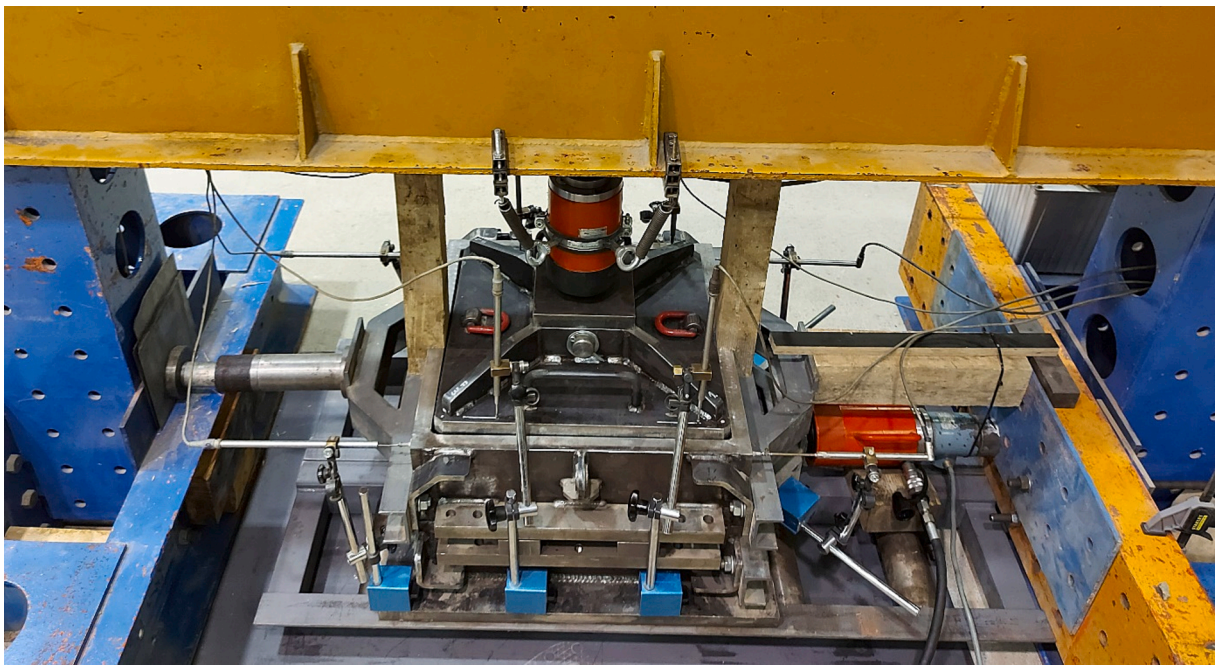

Fig. 6. Photograph of the large-scale shear box apparatus.

initial tests, the upper half was only fixed horizontally. When the aggregate started to dilate after a short compression phase, the upper half was lifted by the forces and a gap was created between the two halves. The gap grew without limits, and the ballast assembly could not be sheared all the way till failure. Two vertical retainer bars were installed to prevent the unlimited growth of the gap, which maximised its size in 3 mm. This maximum gap was reached shortly after the dilation phase started and remained constant thereafter. A definite shear failure occurred in all tests as the result of the modification.

The shear force was measured with a 200 kN (type: MOM-Kaliber 7924, S/N 791274), and the normal force was recorded with a 50 kN (type: MOM-Kaliber, 7924 S/N 781222) force sensor. Because of the gap between the two halves, friction between the shear box parts occurred only at the rollers under the shear cell (excluding the short compression phase, where the friction between the two shear box halves was neglected). This friction was measured in separate tests and was taken into account during the computation of the shear forces. Furthermore, the weight of the upper half was added to the normal force. The normal displacement of the lid was measured with four HBM W20TK (S/N 6950, 6951, 5451 and 5013) inductive displacement sensors. Because of this, not only the average normal displacement, but also the angle of the lid could be computed (three of the four sensors were chosen in each test based on the quality of the position data they provided, and a plane was fitted to calculate the angles of inclination with the horizontal plane). The shear displacement was recorded with two HBM WA100 (S/N 0324141 and 0324144) in pushing and two HBM W50K (S/N 8807 and 8072) inductive sensors in pulling direction, the displacements of which were averaged. The pressure of the hydraulic fluid in the circuit for the normal force was also measured with a 500 bar HBM P4Ak (S/N B155528) pressure sensor to validate the data of the normal force sensor.

Sample preparation

The grains tested in the large-scale shear test were selected from larger assembly according to the classification method introduced in Section “The new aggregate sorting method and its theoretical relation to bounding box-based characterisation systems”. Three assemblies were created from the four different stone types. The target compositions based on mass percentage (m%) were:

- *compact assembly*: 50 m% C31.50/40 and 50 m% C40/50;
- *non-compact assembly*: 50 m% NC31.50/40 and 50 m% NC40/50;
- *mixed assembly* (10:3 compact-to-non-compact grain mass ratio): 11.5 m% NC31.5/40, 11.5 m% NC40/50, 38.5 m% C31.5/40, 38.5 m % C40/50.

In the original, larger assembly, the proportion of the non-compact grains was much lower than the compact ones, therefore about 2.5 tonnes of standard railway ballast were processed until the needed amount was collected. During railway construction, railway ballast is washed before its application to improve frictional properties between particles via the removal of fines, therefore the investigated aggregates were also cleaned. Because industrial equipment was not accessible during the experiments, each grain was manually cleaned under running water using a simple root brush. The stones were placed into the shear cell by hand and were not compacted to avoid layers with different porosity. The second aim with this filling method was to mimic the gravity deposition process frequently applied in simulations. At the end, the top of the assembly was levelled by hand to get more contact points thus a more even force network with the lid of the box. With the applied filling method, the grains in the compact and mixed assemblies had evenly random orientations and the effect of walls was limited as well, because only 1–2 layers of grains aligned with them in their near vicinity (visual inspection). However, grains in the non-compact assembly had high tendency to align with the walls and each other, which made hard to place them in evenly random orientations. A similar behaviour is also expected in industrial scales, when the grains align with each other due to vibrations and disturbances, resulting an assembly with a highly directed fabric. Therefore, special attention was taken when the box was filled with the non-compact assembly: the grains were laid on their flat sides, similarly to how they would align in a larger sample without walls. With this filling method, the shearing happened in the weakest plane of the assembly, when the normal of the flat sides of the grains are orthogonal to the shearing direction. This alignment is favourable, because in realistic, complex load conditions, such an assembly is also likely to fail along its weakest plane.

During the large-scale shear box tests, each type of assembly was

tested under 4 different nominal normal loads (20, 40, 60, 80 kPa for the compact and 20, 30, 40, 50 kPa for the non-compact and mixed assemblies). The final normal stresses were slightly higher because the weight of the upper shear cell half was added to it and there was some scatter due to the analog and manual hydraulic system. Three repetitions were made at each load level, resulting in 12 tests for each aggregate and 36 measurements altogether. The assemblies were reused in the tests corresponding to the same type of composition, because it would require too much effort to sort 12 × 2.5 tonnes railway ballast. Therefore, measures were taken to guarantee comparable but randomised results. The grains were taken out from the shear cell, mixed, and poured back between each test, to generate different initial packings of the same grains. The fines and those grains whose breakage was clearly visible (e.g. broken into half or into multiple pieces) were removed from the assembly and replaced with fresh ones to maintain the same size and form distribution throughout the tests. The normal loads were chosen to keep the breakage rate low (<3 m% in each test). The size and shape ratios, the total mass and grain number were known at the beginning and were measured at the end of all test series for each assembly. The results will be introduced in Section "Evolution of particle form during shear box tests", Table 4. Using the mass of the assemblies (m_s [kg]), and the inner volume of the shear cell (V_c [m^3]), the porosity (ϕ, [-]) was computed as:

$$\phi = \frac{V_c - \frac{m_s}{\rho_s}}{V_c} = 1 - \frac{m_s}{\rho_s V_c} \tag{13}$$

If we omit the error of the mass and volume measurements and the errors due to the limited precision of the measurement equipment, which are much smaller than the uncertainty of the density ($\delta\rho_s = 55$ kg/m^3, approximated by two standard deviations), the uncertainty of the porosity for small deviations is:

$$\delta\phi = \sqrt{\left(\frac{\partial\phi}{\partial\rho_s}\right)^2 (\delta\rho_s)^2} = \frac{m_s}{\rho_s^2 V_c}\delta\rho_s \tag{14}$$

Results

Size characterisation

The PSD of the 100 scanned particles was calculated with the two numeric methods and was compared with the known PSD from sieving in Fig. 7. The piece percentages were calculated in this comparison instead of the typically employed mass percentages, aiming to exclude the influence of deviations in density. This effect is expected to be insignificant for assemblies with large numbers of grains (e.g. >1000) but might influence the results when the number of analysed particles is low. The intermediate dimension method overestimated the size of the ballast grains analysed here, but the diagonal method led to close agreement with the sieve curve.

Using numerical techniques to size the ballast particles can provide additional information from individual particles, beyond the sieve curves of the whole assembly. The errors of the two numeric size characterisation methods can be seen in Table 2, along with their median value and the number of falsely classified grains (n). It becomes evident that the diagonal method performed better in this second comparison as well, hence this technique is recommended over the intermediate dimension method for these analysed ballast particles.

Form characterisation

The form indices of the 100 scanned ballast grains can be seen in Figs. 8 and 9. In Fig. 8, the indices are plotted in a Zingg diagram. The Angelidakis et al. boundaries and the separating lines of the combined bar sieve – shape index calliper method (EN 933-3 and EN 933-4) are also shown. The form index values of most grains that was computed based on 3D imaging data, correspond to their experimental

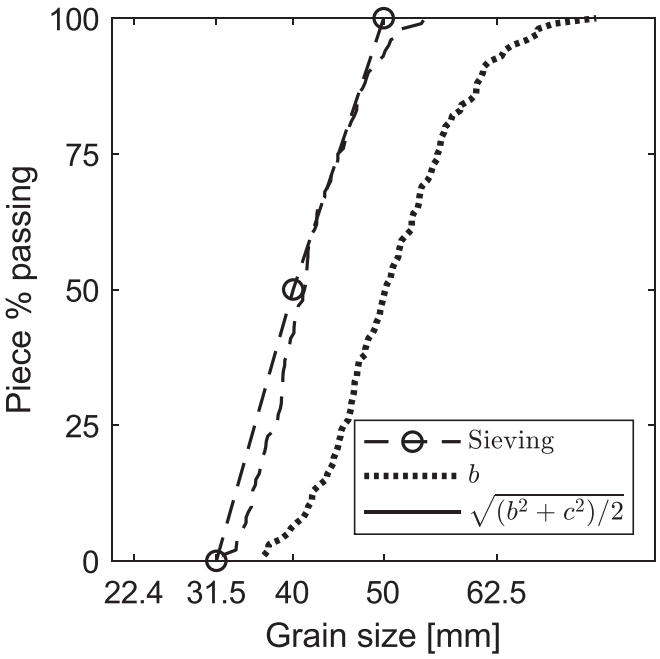

Fig. 7. Particle size distribution (PSD) curves with sieving, based on the intermediate dimension b of the minimal oriented bounding box (OBB) and calculated with the diagonal of the smallest face of the minimal OBB $D = \sqrt{\left(b^2 + c^2\right)/2}$, where c is the small principal dimension of the OBB.

classification, and fall in its respective region. However, there are minor discrepancies. It is interesting to note that almost all grains that fall into the size-dependent zone of the bar sieve are (experimentally) compact, although about an equal number of non-compact and compact grains was expected. Two small compact grains (C31.5/40), which take almost $b/a = 1$ ratios are in the wrong region. An opposing phenomenon is that a few non-compact grains (NC31.5/40 and NC40/50) fall into the compact side of the EN 933-3+4 boundary line. Note that all of them fall along the curve segment of the shape calliper. There are multiple phenomena that can cause these disagreements. Firstly, the agreement between the particle dimensions obtained using the OBB and using the experimental methods is not perfect. E.g., the shape calliper approximates the major size (a) of the OBB as the longest measurable distance on the grain, which can overestimate its value. (Imagine a cube, where its longest distance is its diagonal, which is $\sqrt{3} \approx 1.73$ times larger than the major size of its OBB). Furthermore, the perpendicularity of the principal axes is not guaranteed during the experimental grading procedure. Moreover, irregular and non-convex grains might find a "tricky" way to sneak through the apertures of the different gauges, a behaviour which cannot be captured by the OBB.

It can be seen that variations in form indices are larger in the case of the compact grains, while the non-compact grains have a well-pronounced form. The presence of elongated grains in the sample of 100 grains is low (2–3 grains are elongated from 50 non-compact grains), which supports the practice that flat and elongated grains are not distinguished, in EN 933-3 and EN 933-4 standards.

The medians and error numbers for the 5 introduced methods can be seen in Table 3. Because non-compact grains in the experimental grading procedure also included elongated particles, the error numbers of the different systems were calculated based on the sum of their elongation and flatness indices. The Potticary et al. (ellipsoid-based) indices had the best correspondence with the experimental grading procedure ($\varepsilon = 0.082$ and 2 % falsely classified particles). The Angelidakis et al. method (here applied using the OBB-based main particle dimensions) and the Bagi and Orosz (SOT-based) systems performed equally well with similar error numbers ($\varepsilon = 0.115$ and $\varepsilon = 0.116$, 4 %

Table 2
Median size (m), number of falsely classified grains (n) and error numbers (ε) of oriented bounding box (OBB)-based size characterisation methods.

Sizing method	Median size (m [mm])	Falsely classified particles (n)	Size classification error (ε [mm])
$D = b$	50.28	28	0.9565
$D = \sqrt{\left(b^2 + c^2\right)/2}$	41.30	14	0.3141

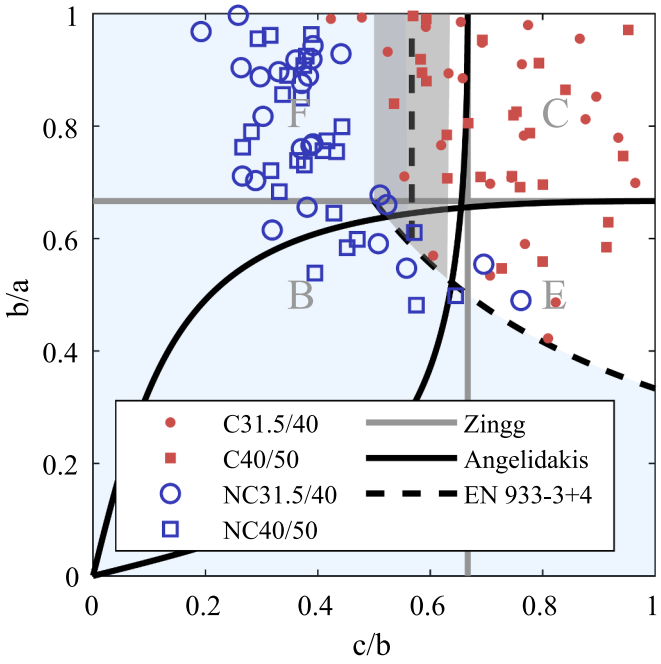

Fig. 8. Zingg plot of the 100 scanned ballast grains, showing the comparison between experimental and digital imaging-based classification of the particles. The marker types indicate experimental classification: C…/…: compact; NC…/…: non-compact per sieve cut (31.5/40; 40/50) and the marker positions indicate imaging-based form index values. The classification systems of Zingg [6], Angelidakis et al. [55] and EN 933 [4,5] are overlaid to facilitate comparisons, where the Zingg the region names are: C: compact, E: elongated, F: flat, B: bladed.

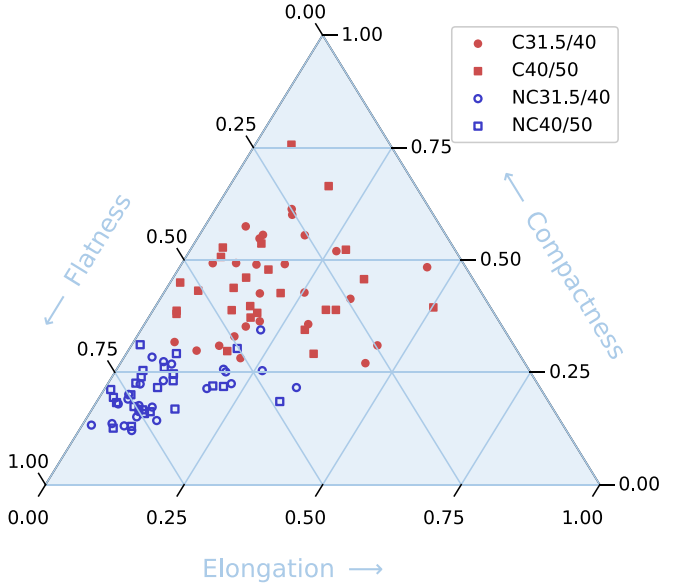

Fig. 9. Ternary plot of the compactness, flatness and elongation values of the 100 scanned grains based on their surface orientation tensor (SOT) [64,65]. The marker types indicate grain size and form according to the combined sorting method (C31.5/40: compact grains from 31.5 to 40 mm, C40/50: compact grains from 40 to 50 mm, NC31.5/40: non-compact grains from 31.5 to 40 mm, NC40/50: non-compact grains from 40 to 50 mm) and the marker positions indicate imaging-based form index values.

and 6 % falsely classified particles, respectively) and had similar error values as the Potticary et al. indices. The Zingg/Kong and Fonseca indices (calculated using the OBB-based main particle dimensions) demonstrated higher, but still reasonable error numbers ($\varepsilon = 0.48$ and 10 % falsely classified particles for both).

Because half of the investigated grains were compact (50 from 100), the computed medians are also functioning as thresholds at which the investigated imaging-based techniques have the best correspondence to the combined standard classification procedure which uses bar sieve and shape index calliper. These thresholds establish a relationship between industrial and laboratory shape classification techniques. The number of the investigated grains were relatively low (100) therefore the medians were rounded to two decimal places. The thresholds, which correspond to the combined bar sieve and shape calliper sorting method are as follows. The grain is non-compact when the sum of the elongation and flatness indices is:

- smaller than 1.28 (computed with the Zingg method [6]), or
- larger than 0.72 (computed with the Kong and Fonseca method [62]), or
- larger than 0.45 (computed with the Angelidakis et al. method [55]), or
- larger than 0.58 (computed with the Potticary et al. method [63]), or
- larger than 0.71 (computed with the Bagi and Orosz method [64]).

Table 3
Median elongation + flatness value (m), number of falsely classified grains (n) and error numbers (ε) of the form characterisation methods and the proposed thresholds for elongation and flatness based on the half of the medians ($m/2$).

Form characterisation method	Median elongation + flatness (m)	Falsely classified particles (n)	Form classification error (ε)
Zingg [6]	1.283	10	0.483
Kong and Fonseca [62]	0.717	10	0.483
Angelidakis et al. [55]	0.454	4	0.115
Potticary et al. [63]	0.581	2	0.082
Bagi and Orosz [64]	0.706	6	0.116

Evolution of particle form during shear box tests

The average density of the grains was measured using Archimedes' principle and was found to be $\rho_s = 2541 \pm 55$ kg/m^3 (two standard deviations, 25 repetitions were made with 2–3 kg samples, the two smallest and two largest values were removed). The size of the grains decreased during shearing due to the breakage of their corners: at the end of all 12 tests with each assembly, the ratio of the 22.4/31 grains increased from 0 m% to 4.06 m%, 12.05 m% and 4.41 m% in the case of the compact, non-compact and mixed assembly, respectively. All compact grains remained compact in the compact assembly, however 10.58 m% of the non-compact grains become compact in the non-

Table 4
Initial and final aggregate properties.

Assembly		Compact m% (pc %)			Non-compact m% (pc %)			Total mass [kg]	Total grain number	Porosity [-]
		22.4/31.5	31.5/40	40/50	22.4/31.5	31.5/40	40/50			
Compact	Initial	0	50.18 (61.82)	49.82 (38.18)	0	0	0	109.326	1079	0.455 ± 0.012
	Final	4.06 (6.83)	48.30 (57.53)	47.64 (35.64)	0	0	0	96.762	996	0.462 ± 0.012
Non-compact	Initial	0	0	0	0	49.96 (63.55)	50.04 (36.45)	109.214	1306	0.442 ± 0.012
	Final	1.88 (3.10)	4.40 (4.46)	1.30 (0.80)	7.99 (12.81)	35.81 (43.68)	48.62 (35.16)	104.854	1257	0.438 ± 0.012
Mixed	Initial	0	38.39 (45.57)	38.45 (27.07)	0	11.54 (16.86)	11.62 (10.50)	104.24	1038	0.474 ± 0.012
	Final	3.09 (4.70)	29.40 (35.13)	42.25 (31.31)	1.32 (2.35)	11.09 (15.75)	12.85 (10.76)	100.184	1022	0.470 ± 0.012

*The mean properties were calculated from sieving data before and after the test series with each type of aggregate, excluding porosity, which was known in each test (m%: mass percent, pc %: piece percent).

compact assembly, which shows that the non-compact grains tend to become compact when they break. This observation is in line with the theory of Buscarnera and Einav [72], who proposed that the shape of the grains tend towards a not too compact (b/a = c/b ≈ 0.70–0.80 with the investigated mechanical parameters) when they break. Contrarily, the ratio of the compact grains had a slight decrease from 76.84 m% to 74.74 m% in the mixed assembly. The ratio of the non-compact grains did not decrease, because they tended suffer bulk breakage in the mixed assembly, therefore they were removed and replaced with new ones. A few compact grains broke as well, and they might have been replaced with non-compact ones which explains why their proportion increased. Despite the small differences in the composition of the assemblies between each test, the shear strengths did not show any progressive trend (i.e. the shear strength was not affected by the number of the test and varied randomly), therefore the results were decided to be comparable.

Macromechanical behaviour of the uniaxial compression stage

Each shear test started with the application of the normal load. During this compaction phase, neither the velocity, nor the force increment was constant, therefore stress–strain graphs could not be recorded. However, the compactions after the application of the normal loads contain valuable information. Fig. 10 shows the normal stresses [kPa] and normal strains [%] for each assembly and load level. The data of the corresponding repeated tests were averaged. Standard deviations were not computed due to the low number of repetitions (3 for each setting). It can be seen that the grain form had no noticeable effect on the compressive behaviour of the assemblies in the measured load ranges. The relationship between the normal stress and normal strain is roughly linear. Cracking sounds of grain breakage was not observed at this phase of the test.

Macromechanical behaviour of the shearing stage

The shear behaviour of the assemblies in individual tests was compared at 44 ± 2 kPa normal stress. (The normal stress had small variations due to the tolerance of the manual hydraulic system. For the chosen three tests, two standard deviations of the variation are computed.) Typical results for each type of assembly can be seen on Figs. 11–14. The shear stress [kPa] is shown in Fig. 11, while Fig. 12 demonstrates the average normal strain of the lid [%] and Figs. 13 and 14 indicate change in its different angles [°] vs. the shear strain [%]. The apparatus was originally designed to be able to attain 60 mm of shear displacement (i.e., 12 % shear strain), but it turned out to be capable of larger movements with some modifications. The displacement sensors were replaced and the screws to create the gap between the two shear box halves were removed, because they were not necessary. The tests

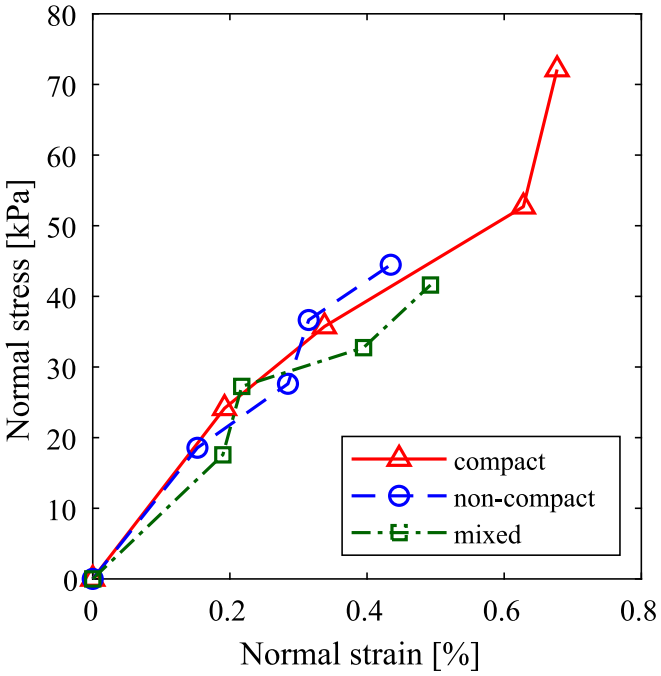

Fig. 10. Averaged normal stress [kPa] vs. normal strain [%] values of the three different assemblies at the end of the initial compaction phase of the shear box tests (three repetitions at each normal stress).

were continued beyond that value until a physical limit was reached (e.g., the cell clashed with one of the sensors or a sensor stand). There were slight differences in the setups between the measurement due to the reposition of the displacement sensors hence the maximal shear strain also varied. The normal displacement sensors failed at about 8 % shear strain during the 44 ± 2 kPa compact tests, therefore the corresponding curves on Figs. 12, 13 and 14 are shorter.

The development of the shear stresses (Fig. 11) showed a roughly linear increase, followed by a distinctive point indicating material failure (e.g., see the compact assembly at about 8 % shear strain), after which shear stress oscillated about a constant value. This behaviour corresponds to a loose assembly. The material showed compression at the beginning of the shearing, which turned into dilatational behaviour at about 2 % shear strain, after reaching a minimum at height at about 1 % shear strain. It is interesting to note that this pattern usually belongs to dense granular media which is the opposite what the shear stress results show. This behaviour is similar to the literature results e.g. [44,51]. The only difference is that, in the literature, the shear stress had

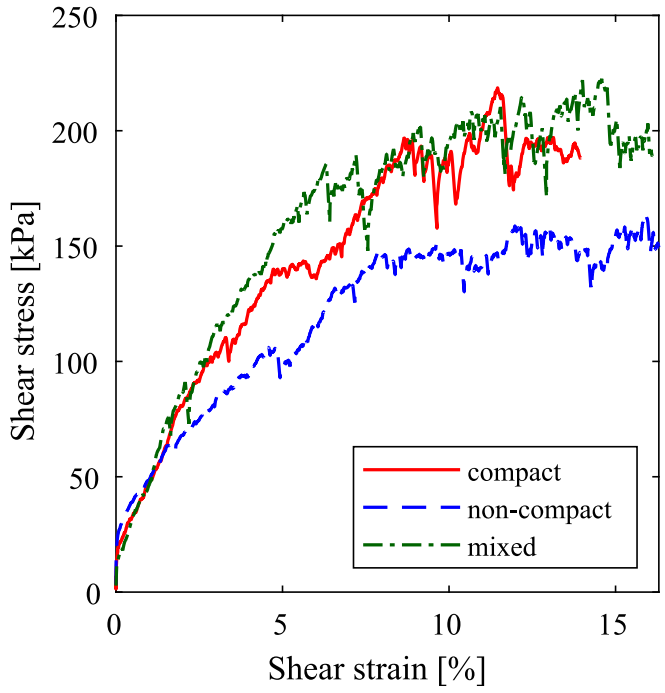

Fig. 11. Shear stress [kPa] – individual shear strain [%] graphs for a compact (2nd from 3), a non-compact (3rd from 3) and a mixed assembly (3rd from 3) at 44 ± 2 kPa normal stress.

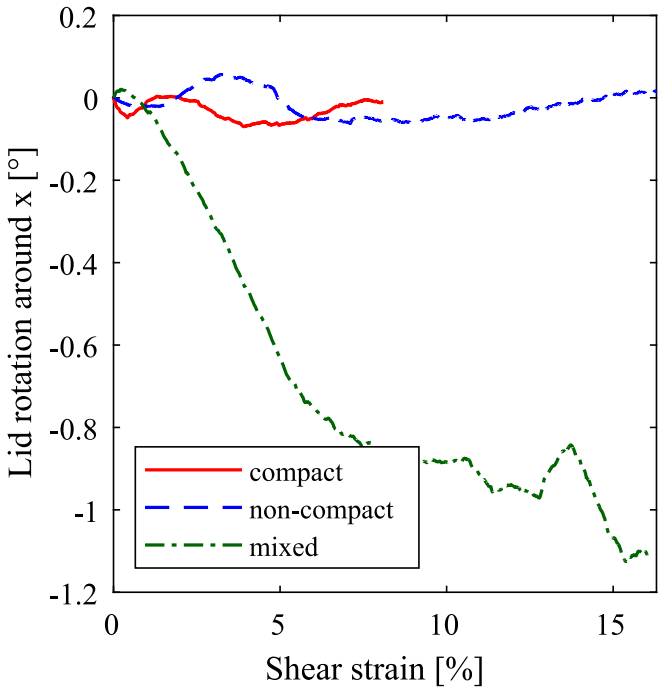

Fig. 13. Lid rotation around x axis [°] – shear strain [%] graphs for a compact (2nd from 3), a non-compact (3rd from 3) and a mixed assembly (3rd from 3) at 44 ± 2 kPa normal stress.

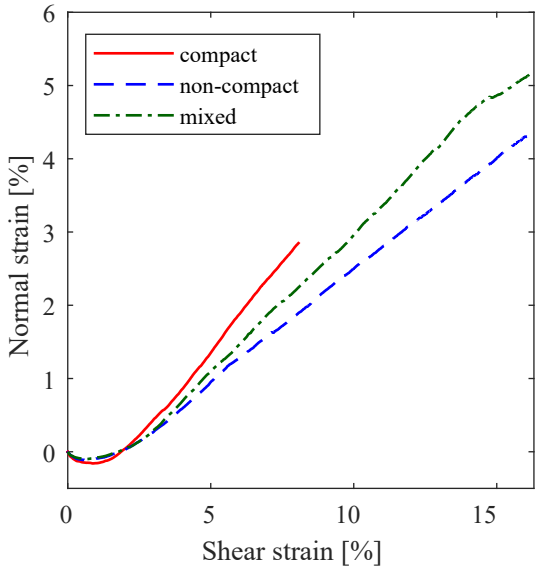

Fig. 12. Normal strain [%] – shear strain [%] graphs for a compact (2nd from 3), a non-compact (3rd from 3) and a mixed assembly (3rd from 3) at 44 ± 2 kPa normal stress.

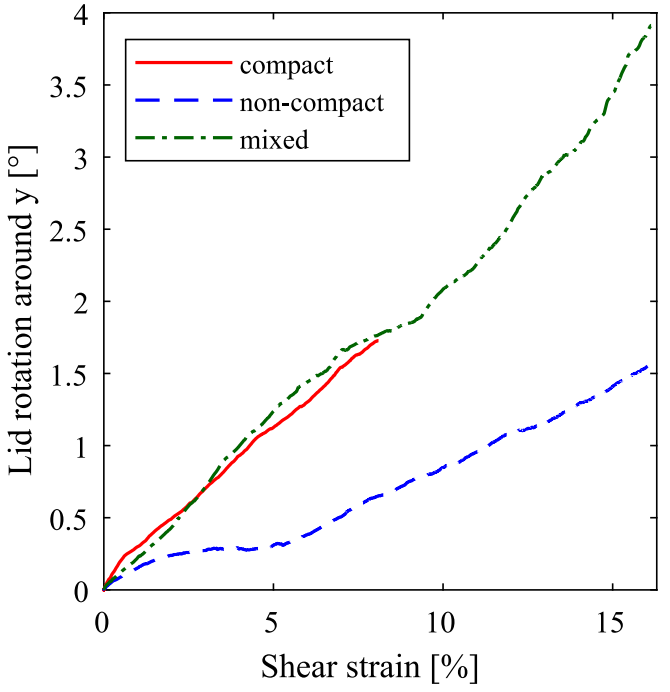

Fig. 14. Lid rotation around y axis [°] – shear strain [%] graphs for a compact (2nd from 3), a non-compact (3rd from 3) and a mixed assembly (3rd from 3) at 44 ± 2 kPa normal stress.

slight monotonous decrease after reaching the peak shear strength instead of keeping a constant average value. The lid rotation around the x axis (Fig. 13) did not how any monotonous trend. Although it became −1° in the case of the mixed assembly at the studied test, other test showed smaller and random deviations from zero. However, the lid rotation around the y axis (Fig. 14), increased linearly in every case.

Because the individual tests showed high amount of scatter, averaged and smoothed graphs were also computed to make the comparison of the shear behaviour of different assemblies and load levels easier. Firstly, the datapoints were interpolated to have common shear strain values, then their mean average was computed. The averaged graphs were then smoothed by computing their moving average. The results are shown in Figs. 15–18. The oscillations, which were caused by grain breakage and sudden rearrangements of the assembly, disappeared in the smoothed graphs.

The normal stresses between different tests were not exactly the

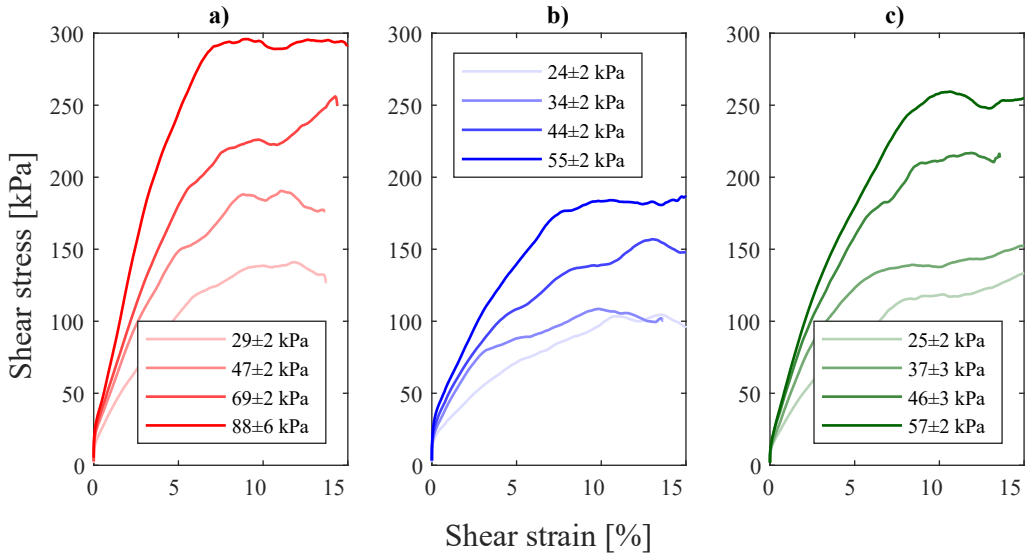

Fig. 15. Averaged shear stress [kPa] – shear strain [%] graphs for all test at different normal stress levels: a) compact, b) non-compact, c) mixed assembly.

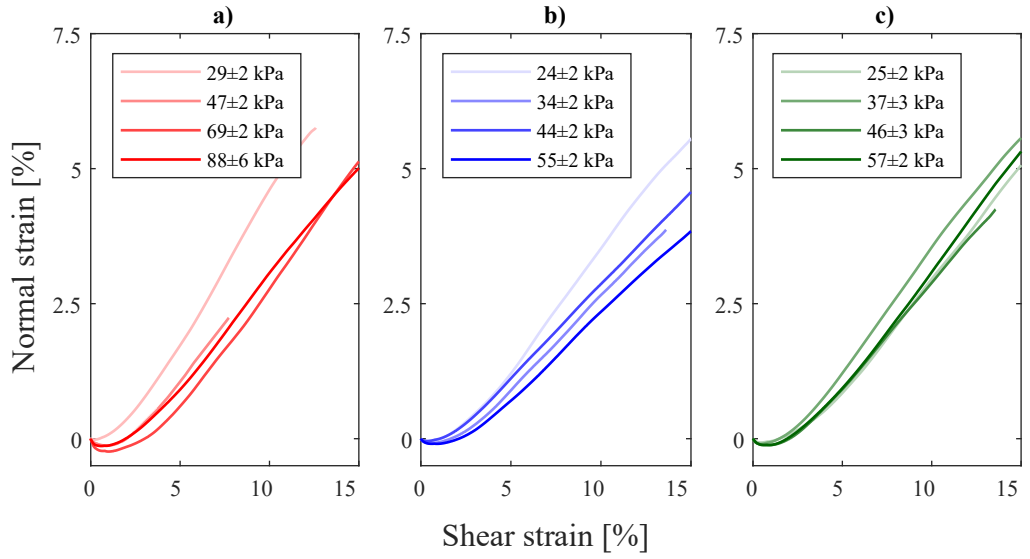

Fig. 16. Averaged normal strain [%] – shear strain [%] graphs for all test at different normal stress levels: a) compact, b) non-compact, c) mixed assembly.

same (Figs. 15–18) (and differed from the normal stresses in the individual tests as well), because their value could not be precisely adjusted due to the manual hydraulic system, but the results are still comparable, due to the small amount of the differences. The shear stress increases with increasing normal stress (Fig. 15), as expected. The normal strain (Fig. 16) and the lid rotation (Fig. 18) decreased slightly for increasing normal load.

Regarding the effect of grain form, the mixed assembly exhibited the highest shear strength (Fig. 15) considering the normal stress and the compact was the second. This proves the hypothesis that the non-compact grains strengthen the assembly at the studied load level up to a certain ratio. The non-compact assembly was the weakest. This can be attributed to the fact that the grains were highly oriented (it was an observation that flat grains tend to naturally align that way, and the same orientation is expected in bigger assemblies, especially if they were subjected to vibrations), and the shearing happened in the weakest direction of the assembly, therefore sliding planes could be easily developed without significant interlocking of the non-compact grains. Grain form had no noticeable effect on the compaction-dilation of behaviour (Fig. 16), but it affected the y component of the lid rotation (Fig. 18). The lid rotation was the highest for the non-compact assembly, the lowest for the mixed assembly and in between the two for the compact assembly. This is exactly the opposite of the shear strength behaviour, however it would require further analysis to be able to state that higher shear strength always comes with lower lid rotation. The averaged results of the lid rotation around the x axis (Fig. 17) also shows that there were no monotonous trend in the variation of that component.

Fig. 19 shows the measured shear strengths [kPa] of each assembly at each normal load [kPa]. The strengths were calculated in two ways: Fig. 19 a) shows the maximum shear stresses and the corresponding normal stress at that moment, while Fig. 19 b) represents the averaged shear and normal stresses from failure of the assembly until the end of the test. The error bars represent two standard deviations. Mohr-Coulomb lines were fitted on the datapoints, whose internal friction angle and apparent cohesion values are listed in Table 5. Note that according to Xu and Xu [73], the Mohr-Coulomb criterion cannot describe the shear strength well when particle breakage is considered. However, this criterion was applied in this study because the proportion of broken

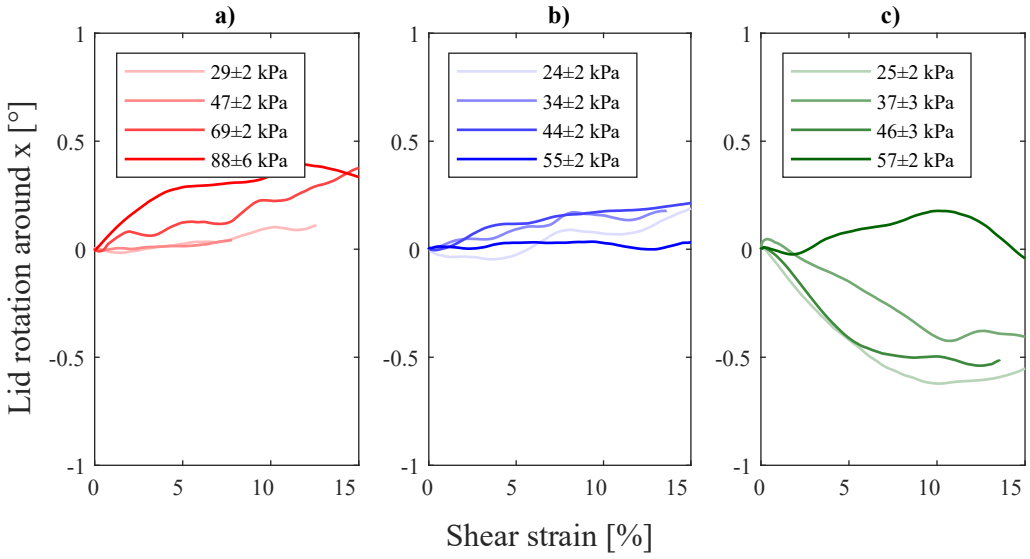

Fig. 17. Averaged lid rotation around x axis [°] – shear strain [%] graphs for all test at different normal stress levels: a) compact, b) non-compact, c) mixed assembly.

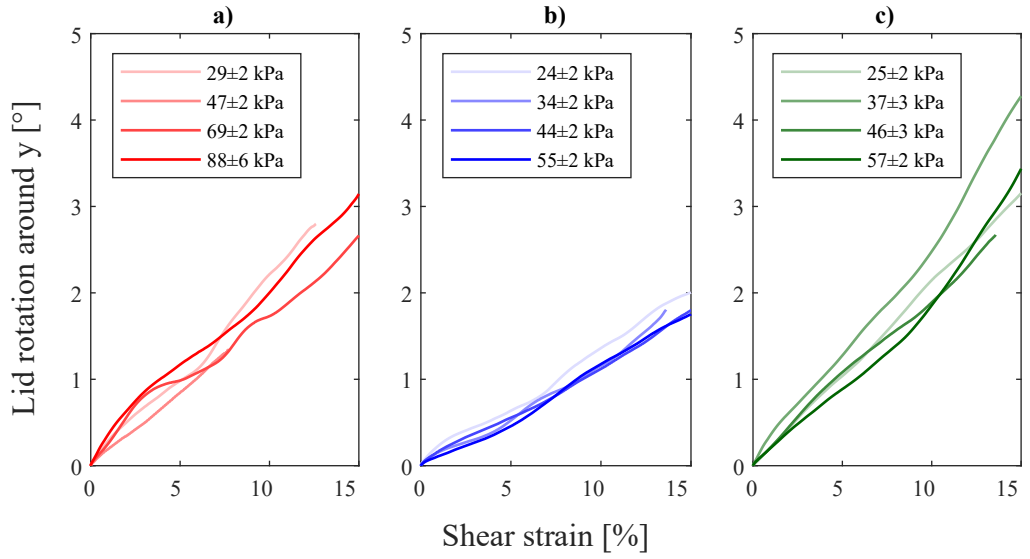

Fig. 18. Averaged lid rotation around y axis [°] – shear strain [%] graphs for all test at different normal stress levels: a) compact, b) non-compact, c) mixed assembly.

grains was low in all tests.

The mixed assembly had the highest internal friction angle with 77.63° ($R^2 = 0.79$) for the maximum shear stress, and 77.05° ($R^2 = 0.83$) for the mean shear stress computation method, proving the hypothesis, that the mixed assembly has the greatest resistance against shear. The non-compact assembly had the second highest friction angle with 72.04 ($R^2 = 0.83$) and 71.59° ($R^2 = 0.84$) value, and the smallest values belonged to the compact assembly with 69.89° ($R^2 = 0.87$) and 68.83° ($R^2 = 0.89$). The mixed and non-compact assemblies had apparent cohesions close to zero, especially for the averaged results, which is expected in the case of cohesionless materials. However, the compact assembly had a much higher apparent cohesion of 74.58/59.81 kPa, making it the second strongest material in the studied load region despite that it had the lowest internal friction angle.

Grain breakage during shearing

The mass of the crushed grains and fines was measured to examine if breakage was kept low during the tests. Fig. 20 shows the average broken masses per normal stress and assembly (standard deviation was not computed due to the low repetition number, which was 3). The compact assembly had the least amount of breakage, even though it was subjected to higher loads than the non-compact and mixed assembly. The non-compact assembly suffered the most breakage, which is not surprising as it was made of vulnerable, mostly flat grains. The mass of broken grains in the mixed assembly was almost as high as the fully non-compact assembly. Furthermore, it was observed that the majority of the broken grains were non-compact. Linking this to the high shear strength of the mixed assemblies, the following hypothesis can be made: the non-compact grains are found in between the compact grains and provide interlocking. That is why, this assembly has the highest internal friction angle. However, due to the same mechanism, the non-compact grains are subjected to high forces and break first, in comparison to the compact ones.

The breakage patterns of the grains contain valuable information for the development of DEM models. 149 broken grains were recovered from which 144 split into two halves. This split was asymmetric in 89 cases (Fig. 21 a) and went through roughly the centroid 55 times (Fig. 21

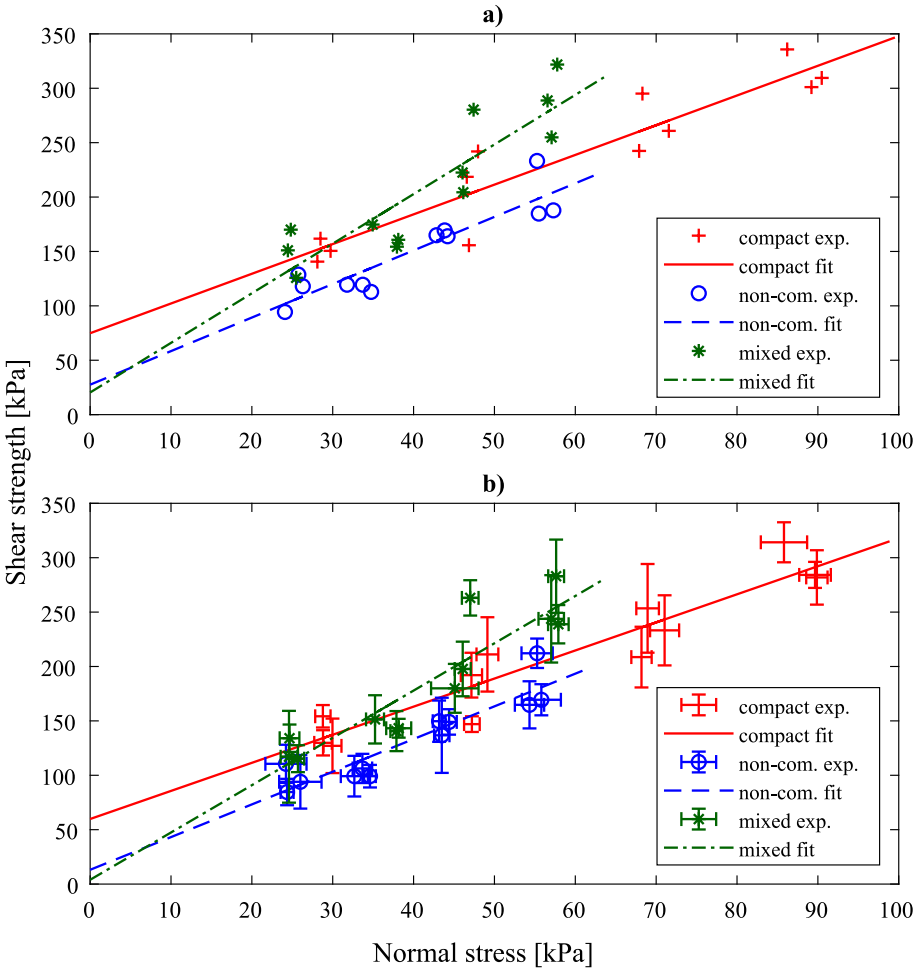

Fig. 19. Mohr-Coulomb failure envelopes for different assemblies (exp. = experiment), computed from the a) maximum shear stress and the normal stress at this stress, b) the averaged shear stress after yield and the averaged normal stress after that point.

Table 5
Mohr-Coulomb failure properties of each assembly.

Assembly type	Shear strength computation method	Internal friction angle [°]	Apparent cohesion [kPa]	R^2
Compact	Max.	69.89	74.85	0.87
	Mean	68.83	59.81	0.89
Non-compact	Max	72.04	27.54	0.83
	Mean	71.59	13.13	0.84
Mixed	Max.	77.63	20.37	0.79
	Mean.	77.05	3.94	0.83

b). The rest 5 pieces of the stone had minimum two perpendicular splitting planes (Fig. 21 c).

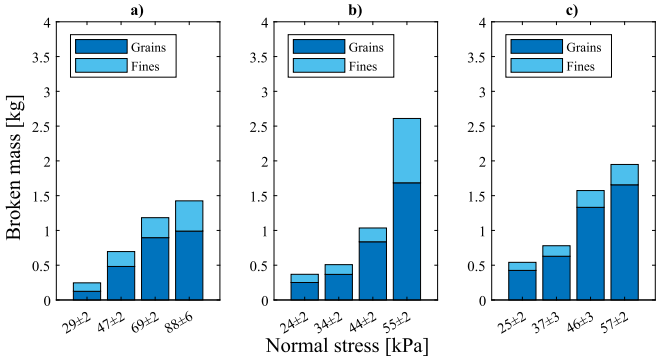

Fig. 20. Average mass of broken grains and fines [kg] per normal stress [kPa] for a) compact b) non-compact and c) mixed assemblies.

Discussion

The introduced form sorting method allows the relatively efficient division of compact and non-compact grains while being closer to the system of Zingg than other standard methods. The "relatively efficient" means that its speed is between the bar sieve and the shape index calliper methods, and it can be used for laboratory-scale samples, but not for industrial quantities. That does not pose a problem, because usually form characterisation in the industry is only used as a quality check measure. If the amount of non-compact grains in the samples exceeds what it specified in the standards, the settings of the processing machines are adjusted until the product meet the requirement. The imaging-based methods gave detailed information about the results of the sorting method, while the established criterion numbers allow to reproduce the sorting method virtually, either on 3D scanned grains or algorithmically generated samples.

The compression phase of the shear box tests did not reveal any dependency on grain form. However, it is widely known from the literature (e.g. [74]) that grain shape does have an effect on the uniaxial compression characteristics of granular materials. The reason that the results did not show any of that behaviour is the relatively low load compared to the large stiffness and strength of the andesite grains. It

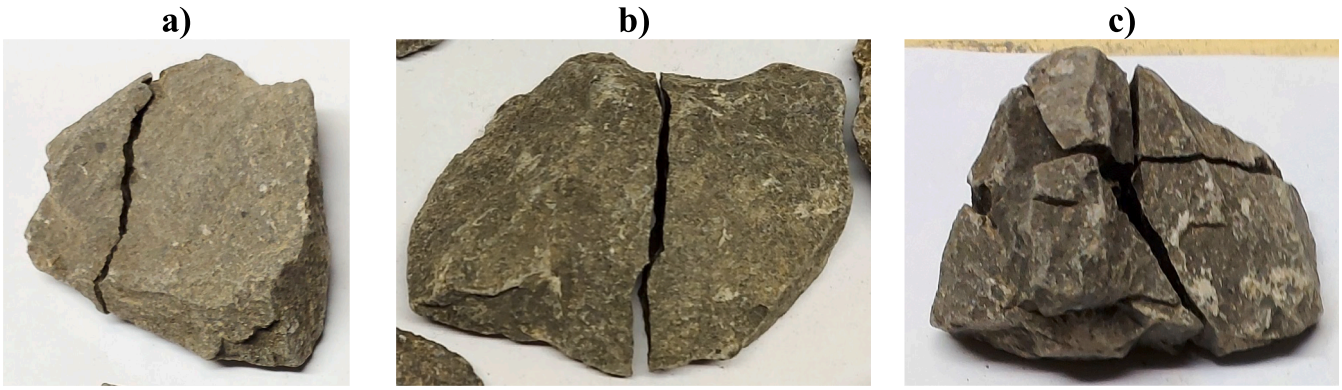

Fig. 21. Different breakage patterns: a) asymmetric split of a flat, b) split through the centroid of a flat c) split along two perpendicular planes of a compact grain.

could have also played a role that the measurement apparatus had not been designed originally for uniaxial compression text, but for shearing of the assembly. E.g., neither the force increment, nor the displacement increment was constant during the tests. Although form dependency could not have been observed, the data of the uniaxial compression phase still contain valuable information for the calibration of elastic modulus-related micromechanical parameters of DEM models.

The shear results clearly show that the mixed assembly has the highest internal friction angle (77.63/77.05°). The internal friction angles of the compact assembly was the lowest (69.89/68.83°) closely followed by the non-compact assembly (72.04/71.59°). Compared with literature data of similar assemblies (50.1–56.3° for Coetzee [44], 53.5–64.6° for Suhr et al. [45], 53.5–64.6° for Linero-Molina et al. [43], 31° for Huang and Tutumluer [46] and 48–65° for Indraratna et al. [51]), it can be seen that the internal friction angles are much higher in this study than any of the literature data, therefore the validity of the results were thoroughly investigated. If there is an issue with the value of the forces, it can either because of a faulty or badly configured sensor (s) or design issue(s) of the apparatus.

The former possibility was investigated firstly. Posterior calibration was carried out for the two sensors. Their measurement range was divided into 10 even parts and 5 repetitions were carried out. The detailed results can be seen in Section 1 of the supplementary material. It was verified by the results that the applied calibration tables based on the factory specifications of the cells were proper, although they were a bit too simple, because only two points were given. The hydraulic pressure in the circuit of the normal force was measured, and the geometrical properties of the cylinder was known, hence the force values measured by the sensor could be easily compared to the ones computed from the hydraulic pressure. All tests were checked, of which a few randomly chosen ones can be seen in Section 2 of the supplementary material. A good correspondence was observed with minor differences. The force measured by the sensor sometimes also had a slight delay compared to the hydraulic pressure, especially at low normal stresses. The main reason of this behaviour is the inner friction of the hydraulic cylinder and other energy losses, which is normal and was expected. There was no pressure gauge in the hydraulic circuit for the shear stress, however there is another opportunity for verification, because the shear cell was different during the preliminary tests of the device: it was a 50 kN MOM-Kaliber 7924 instead of the final 200 kN MOM-Kaliber 7924 cell. The two different cells give similar shear forces at the same normal force (Section 3 of the supplementary material), hence they verified each other.

The next feasibility for errors is an issue with the design of the shear apparatus. The shear force is affected by friction of the rollers, or at other unexpected interface where two faces slide on each other, but that effect was measured (supplementary material Section 4) and accounted. Two vertical wooden beams were placed between the upper half of the shear cell and the reaction frame, which might have exerted extra normal force above the normal hydraulic cylinder. However, this force could only be transferred via the interface between the rocks and the steel wall of the cell, where the coefficient of friction low. As this interface also transmits the weight of the upper half to the assembly (which was added to the normal force), most its load transmission capacity is expected be already exploited, hence this extra force is likely low. The shear strength of the assembly depends on the gap between the shear cell halves [43], the effect of which was not tested. Another feasibility is that even though the minimal recommended cell size for the tested aggregate according to ASTM D3080 was kept, the cell was still too small. E.g., Coetzee [44], whose load ranges and cell size was the closest to our tests, used aggregates up to only 40 mm of grain size, whereas the grain size in our study went up to 50 mm. The effect of cell size can be studied with numerical simulations, where the model is calibrated based on the results presented of this study. Another phenomenon that can account is that internal friction angle is usually larger at low normal stresses.

It is also a possibility that simply the aggregate was so different from the existing ones. The sliding friction angle of the andesite grains was measured to be about 45° in simple inclined slope tests, but the internal friction angle can be much higher due to the interlocking effect. All the studies in literature used real or scaled-down real railway ballast assemblies. Contrarily, here all grains were thoroughly classified and cleaned, and the assemblies were artificially assembled to have the most amount of control over particle size and form distribution. The smallest grain sieve size was 22.4 mm, but the major proportion of the grains were between 31.5 and 50 mm, therefore fines were not present in the tests. The ballast material (andesite) was also different than in any of the previously conducted experiments. Fischer measured the unsorted version of the same aggregate as in our tests using a $1 \times 1 \times 1$ m shear box in his PhD dissertation [47]. The cell was horizontally segmented, there were 9 evenly distributed possible shear planes, 10 cm apart from each other. There was no external normal load in his tests, however the assembly was sheared along all of the upper 4 shear planes, resulting a varying load from the self-weight of the aggregate. These data were used to approximate the internal friction angle in his tests (Section 5 of supplementary material) which was 70.7°, proving that it is not impossible to attain such a high internal friction angle at low normal stress for the tested assembly.

In summary, the high internal friction angles were likely caused by the combined effects of cell size, cell gap, low load and the nature of the ballast materials itself. Even though the test specifications could be improved to better approximate an ideal case without boundary conditions, the main aim of the study, which is to compare assemblies with different grain form can be fulfilled, because the different aggregates were tested under the same conditions. The results can also be used to calibrate numerical models with same boundary conditions then apply the same material under different boundary conditions.

The results of breakage fulfilled the expectations, because it was seen that the breakage rate was kept low and the non-compact aggregate was the most vulnerable.

Conclusions and outlook

The main conclusions of the studies in connection with particle form are as follows.

- Considering Zingg's classification system as reference, the standard bar sieve method (EN 933-3) does not characterise the elongated particles as non-compact. The shape index gauge (EN 933-4) identifies the elongated grains, but it classifies a significant proportion of flat and elongated grains as compact. Therefore, when elongated grains are present in the assembly, a new, combined method is advised, using the bar sieve as the first and the shape index calliper as the second step. This new method performs better in separating the non-compact grains from compact ones, while being relatively fast. However, it has to be considered that the combined method still characterises a small portion of the flat and the considerable portion of the elongated grains as compact.
- Of the two investigated imaging-based size characterisation methods, the one that estimates the size of the grains as $\sqrt{b^2 + c^2/2}$, where b is the length of the intermediate and c is the smallest principal length of the oriented bounding box based on smallest volume, had the best correspondence with the standard industrial sorting process using sieves with square apertures.
- Of the investigated imaging-based form classification methods, the system of Potticary et al. [63] (using fitted ellipsoid) had the closest results to the applied combined standard method. The methods of Angelidakis et al. [55] (here applied using oriented bounding box) and Bagi and Orosz [64,65] (based on surface orientation tensor) performed almost equally well. The system of Fonseca et al. [60] is applicable as well, but it has higher degrees of deviation.

This study compared a few of the common standard industrial and imaging-based form characterisation techniques using a 100-grain sample. The precision of the suggested threshold numbers can be improved by using a larger sample. The introduced workflow in this paper is applicable to other form characterisation systems and different types of grains. The large-scale shear box tests lead to the following conclusions:

- The grain form had no effect on the compression modulus of the assemblies in the studied normal load range, where particle breakage did not occur.
- The mixed assembly, which contained 23 mass% non-compact (of which the majority of the stones were flat) and 77 mass% compact grains had higher resistance against shear than the assemblies containing only compact or only non-compact (majorly flat) particles. Therefore, mixing grains of different forms can have a favourable effect on the shear strength of a railway ballast assembly.

It was demonstrated that andesite railway ballast assemblies with mixed particle shape have the highest resistance against shear in the studied load region, where the breakage is not significant. The optimal ratio of non-compact and compact grains is yet to be found in further research with e.g. DEM simulations. The effect of different grain orientations, especially at non-compact assemblies is also to be investigated. The results of this study offer a point of reference and comparison for parameter calibration and digital shape characterisation.

CRediT authorship contribution statement

Ákos Orosz: Conceptualization, Methodology, Software, Formal analysis, Investigation, Visualization, Project administration, Funding acquisition, Writing – original draft. **Zsolt Farkas:** Investigation, Resources. **Kornél Tamás:** Supervision, Project administration, Funding acquisition, Writing – review & editing.

Declaration of Competing Interest

The authors declare that they have no known competing financial interests or personal relationships that could have appeared to influence the work reported in this paper.

Data availability

Data will be made available on request.

Acknowledgement

Project no. TKP-6-6/PALY-2021 has been implemented with the support provided by the Ministry of Culture and Innovation of Hungary from the National Research, Development and Innovation Fund, financed under the TKP2021-NVA funding scheme. The research has been partially supported by the NKFI OTKA K-138642 grant of the Hungarian Ministry for Innovation and Technology. This paper was supported by the János Bolyai Research Scholarship of the Hungarian Academy of Sciences. The authors express their gratitude to everyone who have contributed the experiments, especially Dr. Dániel Harrach, Prof. Szabolcs Fischer and their colleagues at Széchenyi István University of Győr and Bence Szabó, László Pásthy, Zoltán Hudoba and László Balog from Budapest University of Technology and Economics. Special thanks to Prof. Miklós Gálos and Dr. Vasileios Angelidakis for providing valuable information on the grain shape-dependency of railway ballast aggregates and for motivating this research.

Appendix A. Supplementary material

Supplementary data to this article can be found online at https://doi.org/10.1016/j.trgeo.2023.101105.

References

[1] Mitchell JK, Soga K. Fundamentals of soil behavior. 3rd ed. Hoboken, New Jersey: John Wiley & Sons Ltd; 2005.
[2] Harkness J, Zervos A. Some effects of particle shape on the mechanical behaviour of granular materials. In: Proceeding of the 8th international conference on discrete element methods, Twente, Netherlands; 2019. p. 11.
[3] ISO 3310-1:2016. Test sieves — technical requirements and testing — Part 1: test sieves of metal wire cloth. Standard; 2016.
[4] EN 933-3:2012. Tests for geometrical properties of aggregates. Part 3: determination of particle shape. Flakiness index. Standard; 2012.
[5] EN 933-4:2008. Tests for geometrical properties of aggregates. Part 4: determination of particle shape. Shape index. Standard; 2008.
[6] Zingg T. Beitrag zur Schotteranalyse. Doctoral Thesis. ETH Zürich; 1935. https://www.research-collection.ethz.ch/handle/20.500.11850/135183.
[7] Sefi F, Lav MA. Evaluation of a new grain breakage factor based on the single grain crushing strength. Transp Geotech 2022;33:100733. https://doi.org/10.1016/j.trgeo.2022.100733.
[8] Tutumluer E, Rao C, Stefanski JA. Video image analysis of aggregates. Urbana, Illinois: University of Illinois at Urbana-Champaign; 2000. http://hdl.handle.net/2142/46350.
[9] Zhao L, Zhang S, Deng M, Wang X. Statistical analysis and comparative study of multi-scale 2D and 3D shape features for unbound granular geomaterials. Transp Geotech 2021;26:100377. https://doi.org/10.1016/j.trgeo.2020.100377.
[10] Ying M, Liu F, Wang J, Wang C, Li M. Coupling effects of particle shape and cyclic shear history on shear properties of coarse-grained soil–geogrid interface. Transp Geotech 2021;27:100504. https://doi.org/10.1016/j.trgeo.2020.100504.
[11] Namjoo AM, Baniasadi M, Jafari K, Salam S, Mohsen Toufigh M, Toufigh V. Studying effects of interface surface roughness, mean particle size, and particle shape on the shear behavior of sand-coated CFRP interface. Transp Geotech 2022;37:100841. https://doi.org/10.1016/j.trgeo.2022.100841.
[12] Anochie-Boateng JK, Komba JJ, Mvelase GM. Three-dimensional laser scanning technique to quantify aggregate and ballast shape properties. Constr Build Mater 2013;43:389–98. https://doi.org/10.1016/j.conbuildmat.2013.02.062.
[13] Xiao J, Zhang X, Zhang D, Xue L, Sun S, Stránský J, et al. Morphological reconstruction method of irregular shaped ballast particles and application in numerical simulation of ballasted track. Transp Geotech 2020;24:100374. https://doi.org/10.1016/j.trgeo.2020.100374.

[14] Jerónimo P, Resende R, Fortunato E. An assessment of contact and laser-based scanning of rock particles for railway ballast. Transp Geotech 2020;22:100302. https://doi.org/10.1016/j.trgeo.2019.100302.
[15] Maroof MA, Mahboubi A, Noorzad A, Safi Y. A new approach to particle shape classification of granular materials. Transp Geotech 2020;22:100296. https://doi.org/10.1016/j.trgeo.2019.100296.
[16] Eller B, Movahedi Rad M, Fekete I, Szalai S, Harrach D, Baranyai G, et al. Fischer, examination of concrete canvas under quasi-realistic loading by computed tomography. Infrastructures. 2023;8:23. doi: 10.3390/infrastructures8020023.
[17] Tolomeo M, McDowell GR. DEM study of an "avatar" railway ballast with real particle shape, fabric and contact mechanics. Granul Matter 2023;25:32. https://doi.org/10.1007/s10035-023-01322-1.
[18] Blott SJ, Pye K. Particle shape: a review and new methods of characterization and classification. Sedimentology 2007;55:31–63. https://doi.org/10.1111/j.1365-3091.2007.00892.x.
[19] Guo Y, Markine V, Zhang X, Qiang W, Jing G. Image analysis for morphology, rheology and degradation study of railway ballast: a review. Transp Geotech 2019;18:173–211. https://doi.org/10.1016/j.trgeo.2018.12.001.
[20] Zhang T, Zhang C, Zou J, Wang B, Song F, Yang W. DEM exploration of the effect of particle shape on particle breakage in granular assemblies. Comput Geotech 2020;122:103542. https://doi.org/10.1016/j.compgeo.2020.103542.
[21] Wei D, Zhao B, Gan Y. Surface reconstruction with spherical harmonics and its application for single particle crushing simulations. J. Rock Mech Geotechn Eng 2022;14(1):232–9.
[22] Kamani M, Ajalloeian R. Investigation of the changes in aggregate morphology during different aggregate abrasion/degradation tests using image analysis. Constr Build Mater 2022;314:125614. https://doi.org/10.1016/j.conbuildmat.2021.125614.
[23] Zheng S-F, Liu Y, Zhang N, Li X, Gao L. Experimental studies on shape and size effects on particle breakage of railway ballast. Transp Geotech 2022;37:100883. https://doi.org/10.1016/j.trgeo.2022.100883.
[24] Cundall P.A. A computer model for simulating progressive large scale movements in blocky rock systems. Procs. symposium of the international society of rock mechanics. Nancy, France; 1971. p. 8.
[25] Bagi K. The discrete element method, Lecture Notes, Department of Structural Mechanics. Budapest: Budapest University of Technology and Economics; 2007.
[26] Shi S, Gao L, Xiao H, Xu Y, Yin H. Research on ballast breakage under tamping operation based on DEM–MBD coupling approach. Constr Build Mater 2021;272:121810. https://doi.org/10.1016/j.conbuildmat.2020.121810.
[27] Przybyłowicz M, Sysyn M, Gerber U, Kovalchuk V, Fischer S. Comparison of the effects and efficiency of vertical and side tamping methods for ballasted railway tracks. Constr Build Mater 2022;314:125708. https://doi.org/10.1016/j.conbuildmat.2021.125708.
[28] EN 13450. Aggregates for railway ballast. Standard; 2002.
[29] Bobály J, Gálos M. Szemalak hatása a vasúti Los Angeles- és a vasúti mikro-Deval vizsgálatok eredményeire. Sínek Világa 2016;58:8–14.
[30] Deiros Quintanilla I. Multi-scale study of the degradation of railway ballast. Université Grenoble Alpes; 2018. PhD dissertation.
[31] Ying M, Wang J, Liu F, Xiong B. Effect of particle regularity on the shear response of geogrid-granular material interface under cyclic normal loading. Transp Geotech 2023;38:100890. https://doi.org/10.1016/j.trgeo.2022.100890.
[32] Liu Y, Gao R, Chen J. Exploring the influence of sphericity on the mechanical behaviors of ballast particles subjected to direct shear. Granul Matter 2019;21:94. https://doi.org/10.1007/s10035-019-0943-1.
[33] Wadell H. Volume, shape, and roundness of rock particles. J Geol 1932;40:443–51. https://doi.org/10.1086/623964.
[34] Talafha MS, Oldal I. Evaluation the effect of particle sphericity on direct shear mechanical behavior of granular materials using discrete element method (DEM). IJEM 2021;34. 10.31534/engmod.2021.1.ri.01m.
[35] Zhao S, Zhao J, Guo N. Universality of internal structure characteristics in granular media under shear. Phys Rev E 2020;101:012906. https://doi.org/10.1103/PhysRevE.101.012906.
[36] Linero-Molina S., Fityus S., Simmons J., Azema E., Estrada N., Dixon J. Influence of particle size-shape correlation on the shear strength of scaled samples of coarse mine waste. In: Proceedings of the 2020 international symposium on slope stability in open pit mining and civil engineering. Perth: Australian Centre for Geomechanics; 2020. p. 667–676. https://doi.org/10.36487/ACG_repo/2025_42.
[37] Indraratna B, Ngo T, Ferreira FB, Rujikiatkamjorn C, Tucho A. Large-scale testing facility for heavy haul track. Transp Geotech 2021;28:100517. https://doi.org/10.1016/j.trgeo.2021.100517.
[38] Horváth D, Tamás K, Poós T. Viscoelastic contact model development for the discrete element simulations of mixing process in agitated drum. Powder Technol 2022;397:117038. https://doi.org/10.1016/j.powtec.2021.117038.
[39] Roessler T., Katterfeld A. Scalability of angle of repose tests for the calibration of DEM parameters. In: Proceedings of international conference on bulk materials storage, handling and transportation (ICBMH 2016), Darwin, Australia; 2016. p. 12.
[40] Wójcik A, Klapa P, Mitka B, Sładek J. The use of the photogrammetric method for measurement of the repose angle of granular materials. Measurement 2018;115:19–26. https://doi.org/10.1016/j.measurement.2017.10.005.
[41] Suhr B, Skipper WA, Lewis R, Six K. DEM modelling of railway ballast using the Conical Damage Model: a comprehensive parametrisation strategy. Granul Matter 2022;24:40. https://doi.org/10.1007/s10035-021-01198-z.
[42] Chen J, Gao R, Liu Y, Shi Z, Zhang R. Numerical exploration of the behavior of coal-fouled ballast subjected to direct shear test. Constr Build Mater 2021;273:121927. https://doi.org/10.1016/j.conbuildmat.2020.121927.
[43] Linero-Molina S, Bradfield L, Fityus SG, Simmons JV, Lizcano A. Design of a 720-mm square direct shear box and investigation of the impact of boundary conditions on large-scale measured strength. Geotech Test J 2020;43:20190344. https://doi.org/10.1520/GTJ20190344.
[44] Coetzee CJ. Calibration of the discrete element method and the effect of particle shape. Powder Technol 2016;297:50–70. https://doi.org/10.1016/j.powtec.2016.04.003.
[45] Suhr B, Marschnig S, Six K. Comparison of two different types of railway ballast in compression and direct shear tests: experimental results and DEM model validation. Granul Matter 2018;20:70. https://doi.org/10.1007/s10035-018-0843-9.
[46] Huang H, Tutumluer E. Discrete Element Modeling for fouled railroad ballast. Constr Build Mater 2011;25:3306–12. https://doi.org/10.1016/j.conbuildmat.2011.03.019.
[47] Fischer S. A vasúti zúzottkő ágyazat alá beépített georácsok vágánygeometriát stabilizáló hatásának vizsgálata, PhD dissertation. Széchenyi István University; 2012.
[48] Horvát F, Fischer Sz, Major Z. Evaluation of railway track geometry stabilisation effect of geogrid layers under ballast on the basis of laboratory multi-level shear box tests. Acta Tech Jaurinensis 2013;6:21–44.
[49] Fischer S. Geogrid reinforcement of ballasted railway superstructure for stabilization of the railway track geometry – a case study. Geotext Geomembr 2022;50:1036–51. https://doi.org/10.1016/j.geotexmem.2022.05.005.
[50] Indraratna B, Ngo NT, Rujikiatkamjorn C. Behavior of geogrid-reinforced ballast under various levels of fouling. Geotext Geomembr 2011;29:313–22. https://doi.org/10.1016/j.geotexmem.2011.01.015.
[51] Indraratna B, Ngo NT, Rujikiatkamjorn C, Vinod JS. Behavior of fresh and fouled railway ballast subjected to direct shear testing: discrete element simulation. Int J Geomech 2014;14:34–44. https://doi.org/10.1061/(ASCE)GM.1943-5622.0000264.
[52] Tanghetti G., Goodey R.J., Divall S., McNamara A.M., McKinley B. Design and development of a large shear box for testing working platform material. In: Proceedings of the XVII ECSMGE-2019; 2019. p. 1425–1431. https://doi/10.32075/17ECSMGE-2019-0267.
[53] Li S, Yang Z, Tian X, Xiao Y, Li X, Liu X. Influencing factors of scale effects in large-scale direct shear tests of soil-rock mixtures based on particle breakage. Transp Geotech 2021;31:100677. https://doi.org/10.1016/j.trgeo.2021.100677.
[54] MSZ 18288-3:1978. Building rock materials. Test for granulometric composition and impurity. Test for grain-form. Standard; 1978.
[55] Angelidakis V, Nadimi S, Utili S. Elongation, flatness and compactness indices to characterise particle form. Powder Technol 2022;396:689–95. https://doi.org/10.1016/j.powtec.2021.11.027.
[56] Sneed ED, Folk RL. Pebbles in the lower Colorado River, Texas a study in particle morphogenesis. J Geol 1958;66:114–50. https://doi.org/10.1086/626490.
[57] EN 565:1990. Test sieves — metal wire cloth, perforated metal plate and electroformed sheet — nominal sizes of openings; 1990.
[58] Chen W, Donohue T, Katterfeld A, Williams K. Comparative discrete element modelling of a vibratory sieving process with spherical and rounded polyhedron particles. Granul Matter 2017;19. https://doi.org/10.1007/s10035-017-0749-y.
[59] Tafesse S, Fernlund JMR, Bergholm F. Digital sieving-Matlab based 3-D image analysis. Eng Geol 2012;137–138:74–84. https://doi.org/10.1016/j.enggeo.2012.04.001.
[60] Fonseca J, O'Sullivan C, Coop MR, Lee PD. Non-invasive characterization of particle morphology of natural sands. Soils Found 2012;52:712–22. https://doi.org/10.1016/j.sandf.2012.07.011.
[61] Ohm H-S, Hryciw RD. Translucent segregation table test for sand and gravel particle size distribution. Geotech Test J 2013;36:20120221. https://doi.org/10.1520/GTJ20120221.
[62] Kong D, Fonseca J. Quantification of the morphology of shelly carbonate sands using 3D images. Géotechnique 2018;68:249–61. https://doi.org/10.1680/jgeot.16.P.278.
[63] Potticary M, Zervos A, Harkness J. An investigation into the effect of particle platyness on the strength of granular materials using the discrete element method. In: Proceedings of the IV international conference on particle-based methods: fundamentals and applications. Barcelona, Spain: CIMNE; 2015. p. 767–79.
[64] Bagi K., Orosz A., editors. A new variable for characterising irregular element geometries in experiments and DEM simulations. In: ECMS 2020 Proceedings edited by Mike Steglich, Christian Mueller, Gaby Neumann, Mathias Walther, ECMS; 2020. p. 256–260. https://doi.org/10.7148/2020-0256.
[65] Orosz Á, Angelidakis V, Bagi K. Surface orientation tensor to predict preferred contact orientation and characterise the form of individual particles. Powder Technol 2021;394:312–25. https://doi.org/10.1016/j.powtec.2021.08.054.
[66] Satake M. Fabric tensor in granular materials. In: Luger VA, editor. Deformation and failure of granular materials. Rotterdam and Delft, Netherlands: A. A. Balkema; 1982. p. 63–8. https://www.scopus.com/inward/record.uri?eid=2-s2.0-0020459819&partnerID=40&md5=aa90f235482c7aec8059391939bc28c6.
[67] Schröder-Turk GE, Mickel W, Kapfer SC, Klatt MA, Schaller FM, Hoffmann MJF, et al. Minkowski tensor shape analysis of cellular, granular and porous structures. Adv Mater 2011;23:2535–53. https://doi.org/10.1002/adma.201100562.
[68] Agrawal N, Nair P, Pöschel T, Roy S. Isotropy of sphere packings in a cylindrical confinement. Chem Eng J 2019;377:119820. https://doi.org/10.1016/j.cej.2018.08.206.
[69] Cignoni P., Callieri M., Corsini M., Dellepiane M., Ganovelli F., Ranzuglia G. MeshLab: an open-source mesh processing tool. In: Scarano V, Chiara RD, Erra U, editors. Eurographics Italian chapter conference. The Eurographics Association;

2008. https://doi.org/10.2312/LocalChapterEvents/ItalChap/ItalianChapConf2008/129-136.
[70] Angelidakis V, Nadimi S, Utili S. SHape Analyser for Particle Engineering (SHAPE): seamless characterisation and simplification of particle morphology from imaging data. Comput Phys Commun 2021;265:107983. https://doi.org/10.1016/j.cpc.2021.107983.
[71] ASTM D3080. Standard test method for direct shear test of soils under consolidated drained conditions; 2011.
[72] Buscarnera G, Einav I. The mechanics of brittle granular materials with coevolving grain size and shape. Proc R Soc A 2021;477(2249).
[73] Xu Y, Xu Y. Numerical simulation of direct shear test of rockfill based on particle breaking. Acta Geotech 2021;16:3133–44. https://doi.org/10.1007/s11440-021-01172-2.
[74] Wiącek J, Molenda M, Horabik J, Ooi JY. Influence of grain shape and intergranular friction on material behavior in uniaxial compression: experimental and DEM modeling. Powder Technol 2012;217:435–42. https://doi.org/10.1016/j.powtec.2011.10.060.